Research Square

Preprints are preliminary reports that have not undergone peer review.
They should not be considered conclusive, used to inform clinical practice,
or referenced by the media as validated information.

Unlocking Catalytic Activity via Tuning Fe 3d Spin State in Fe Dual-Atom Nanozymes with Atomically Dispersed Fe2-N6 Configurations for Reprogramming Immuno-Redox Microenvironment in Rheumatoid Arthritis

Yuntao Liao
Fujian Medical University
Lan Lin
Fujian Medical University
Hong Chen
Fujian Medical University
Jiayu Li
Fujian Medical University
Xiaofeng Liu
Shanghai Sixth People's Hospital
Jiexin Huang
Fujian Medical University
Hongyan Li
Fujian Medical University
Hongxiang Wei
Fujian Medical University
Penghui Wei
Fujian Medical University
Hongjia Zheng
Fujian Medical University
Wenming Zhang
Fujian Medical University
Xinyu Fang
Fujian Medical University
Yang Zhu
zhuyang@mail.ustc.edu.cn

Fujian Medical University

Research Article

Keywords: dual-atom nanozymes, spin state, catalytic therapy, pH-responsive hydrogel, rheumatoid arthritis

Posted Date: August 7th, 2026

DOI: https://doi.org/10.21203/rs.3.rs-10554638/v1

License: This work is licensed under a Creative Commons Attribution 4.0 International License.
Read Full License

Additional Declarations: No competing interests reported.

Unlocking Catalytic Activity via Tuning Fe 3d Spin State in Fe Dual-Atom Nanozymes with Atomically Dispersed Fe_2-N_6 Configurations for Reprogramming Immuno-Redox Microenvironment in Rheumatoid Arthritis

Yuntao Liao[1,2#], Lan Lin[1,2#], Hong Chen[1,2#], Jiayu Li[1,2], Xiaofeng Liu[3], Jiexin Huang[1,2], Hongyan Li[1,2], Hongxiang Wei[1,2], Penghui Wei[4,5], Hongjia Zheng[4,5], Wenming Zhang[1,2]*, Xinyu Fang[1,2]*, Yang Zhu[4,5]*

[1] Department of Orthopaedic Surgery, National Regional Medical Center, Binhai Campus of the First Affiliated Hospital, Fujian Medical University, Fuzhou 350212, Fujian, China.

[2] Department of Orthopedic Surgery, The First Affiliated Hospital of Fujian Medical University, Fuzhou 350005, Fujian, China.

[3] Department of Orthopedics, Jinjiang Municipal Hospital (Shanghai Sixth People's Hospital Fujian), Quanzhou 362200, Fujian, China.

[4] Department of Neurosurgery, Neurosurgery Research Institute, The First Affiliated Hospital, Fujian Medical University, Fuzhou 350005, Fujian, China.

[5] Department of Neurosurgery, National Regional Medical Center, Binhai Campus of the First Affiliated Hospital, Fujian Medical University, Fuzhou 350212, Fujian, China.

* Correspondence: zhuyang@mail.ustc.edu.cn (Yang Zhu); fangxinyu0417@fjmu.edu.cn (Xinyu Fang); zhangwm0591@fjmu.edu.cn (Wenming Zhang).

# These authors contributed equally to this work.

Abstract

Single-atom nanozymes hold great promise for treating reactive oxygen species (ROS)-driven inflammatory diseases, yet their catalytic activity remains limited by unfavorable spin configurations and strong adsorption of reaction intermediates. Here, we report a rational design of high-spin Fe dual-atom nanozymes (HS Fe_2-N_6/DANs) with atomically dispersed Fe_2-N_6 configurations that unlocks superior ROS-scavenging catalytic performance by tuning the Fe 3d spin state, enabling effective reprogramming of the immuno-redox microenvironment in rheumatoid arthritis (RA). Density functional theory calculations verify that HS Fe_2-N_6/DAN exhibits superior hydroxyl radical scavenging, superoxide dismutase-like, and catalase-like activities. The enhanced performance originates from Fe-Fe dual-site coupling, optimized spin density,

and reduced intermediate desorption energy relative to low-spin Fe-N_4 single-atom nanozymes (LS Fe-N_4/SAN). To overcome RA acidic microenvironment-induced activity loss and chondrocyte pyroptosis, we further encapsulated Fe_2-N_6/DANs into a pH-responsive nMgO/Gel hydrogel (nMgO/Gel@Fe_2-N_6/DAN). In vitro and in vivo experiments in a collagen-induced arthritis model confirm that nMgO/Gel@Fe_2-N_6/DAN effectively eliminates ROS, repolarizes pro-inflammatory M1 macrophages into reparative M2 phenotypes, inhibits chondrocyte pyroptosis by suppressing the NF-κB pathway, alleviates synovial inflammation, and maintains cartilage integrity. This triadic design paradigm of 'redox-regulated nanoarchitectures-electronic modulation-biological function' establishes a versatile framework for engineering next-generation spin-dependent single-atom nanozymes for the therapy of ROS-driven degenerative diseases.

Keywords: dual-atom nanozymes, spin state, catalytic therapy, pH-responsive hydrogel, rheumatoid arthritis

1. Introduction

The synovium and cartilage together form a protective barrier for healthy joints. Rheumatoid arthritis (RA), an autoimmune disease, is pathologically defined by the disruption of this barrier, which is manifested as synovial inflammation and progressive cartilage destruction.[1, 2] This disease has become a major public health concern worldwide.[3] During the progression of RA, excessive accumulation of reactive oxygen species (ROS) triggers oxidative damage to the joint barrier, which is specifically reflected in synovial inflammation driven by the accumulation of pro-inflammatory M1 macrophages in synovial tissue, as well as cartilage structural damage mediated by chondrocyte death.[4, 5] Furthermore, activated osteoclasts secrete excessive hydrogen ion (H^+), generating a local acidic microenvironment (pH ≈ 5-6) in RA.[6] The abnormally high H^+ concentration severely interferes with electron transfer at the metal active sites, thereby compromising their antioxidant therapeutic efficacy.[7] Simultaneously, excess H^+ can directly activate the acid-sensing ion channel 1a (ASIC1a) on chondrocyte membranes, mediating a substantial increase in intracellular ROS production and subsequently triggering chondrocyte pyroptosis.[8] However, the therapeutic efficacy of existing antioxidant therapies is significantly limited due to their short duration of action and insufficient catalytic efficiency.

Single-atom nanozymes (SANs), with their well-defined electronic/geometric structures and maximal atomic utilization efficiency, offering a promising strategy to address these limitations.[9-14] Among various SAN architectures, transition metal-nitrogen-carbon (M-N_x-C) configurations are particularly attractive.[15-20] The incomplete d-orbitals of transition metals act as efficient electron acceptance for oxygen-involving intermediates (e.g., O*, OH*, OOH*) generated during ROS scavenging, which substantially lowers the activation energy barrier of redox reactions and enhances overall catalytic activities.[21-24] Specifically, the Fe-N_4 configuration, with a single electron occupying the e_g orbital,[25] has been established as a benchmark SAN active site for ROS scavenging.[26, 27] However, the fundamental mechanism governing the catalytic activity of Fe-N_4 remains incompletely understood, primarily due to the complexity of electronic state of Fe.[28] Importantly, the different orbital interactions between O species and metal sites can profoundly influence the adsorption models, bond dissociation, and adsorption/desorption of intermediates.[29] These interactions, in turn, significantly manipulate both the reaction pathway and kinetics. As a result, the enzymatic performance is highly dependent on the orbital interactions, which are highly sensitive to the spin configurations of the active sites.[30] Given this, the modulation of the spin state is expected to play a crucial role in enhancing the ROS elimination capability. Despite the potential, to the best of our knowledge, the tuning of the spin state of Fe single atoms to amplify catalytic activity remains a significant challenge.

The dynamic interplay of electron occupation and vacancy within the 3d orbitals of Fe is a crucial aspect of ROS elimination.[31] Fundamentally, the Fe-N_4, characterized by its well-defined square planar configuration with D_{4h} symmetry, plays a central role in this process.[32] The Fe 3d orbitals undergo crystal field splitting, yielding two distinct sets: (1) the e_g orbitals ($d_{x^2-y^2}$, d_{z^2}) with two-fold degeneracy, which directly interact with the lone-pair electrons of N atoms in the coordination sphere;[33] and (2) the t_{2g} orbitals (d_{xy}, d_{yz}, d_{xz}) with three-fold degeneracy, which primarily participate in π-back-bonding with oxygen-containing intermediates.[34] The spin-dependent occupancy of these split orbitals (i.e., high-spin (HS) vs. low-spin (LS) states) endows Fe centers with tunable electronic properties, laying the groundwork for modulating catalytic behavior.[35] Several pioneering studies have emphasized that the spin configuration of Fe directly governs the binding strength between the p orbitals of oxygen intermediates and the d orbitals of the Fe active site-an interaction that is particularly critical for catalase (CAT)-like activity.[18, 36] However, symmetry D_{4h} Fe-N_4 configurations

typically exhibits high overpotentials for *OOH desorption, arising from the strong electrostatic interaction between the electron-deficient Fe center and the electron-rich *OOH intermediate.[37, 38] This excessive adsorption strength creates a "surface shielding effect", where occupied active sites are unable to bind new hydrogen peroxide (H_2O_2) substrates, thereby limiting catalytic efficiency.[39] Notably, spin state modulation exerts an even more profound impact on catalytic performance: by altering the occupancy of e_g/t_{2g} orbitals (e.g., increasing the population of unpaired electrons in t_{2g} orbitals), spin tuning directly modulates the strength of adsorbate-catalyst interactions and the activation energy of the rate-determining step (RDS).[40] To the best of our knowledge, leveraging the Fe spin state as a predictive descriptor to guide the rational design of Fe-based SANs for ROS elimination remains an emerging and underexplored research frontier.

Herein, we initially employed a binuclear Fe precursor (dihexylferrocene, $Fe_2(CO)_9$) and a mononuclear Fe precursor (ferric acetylacetonate, $(Fe(acac)_3$) to controllably synthesize two Fe-based nanozymes: Fe dual-atom nanozymes (Fe_2-N_6/DANs) with Fe_2-N_6 binuclear active sites and Fe single-atom nanozymes (Fe-N_4/SANs) with Fe-N_4 mononuclear active sites (Fig. 1). Structural characterization and spin state analysis confirmed distinct electronic configurations for the two nanozymes: the Fe-N_4/SANs adopted a LS state with the electron occupancy of $t_{2g}^4e_g^1$ electron configuration (d_{x2-y2}^1, d_{z2}^0, d_{xz}^2, d_{yz}^0, d_{xy}^2), whereas the Fe_2-N_6/DAN exhibited a HS state with $t_{2g}^3e_g^2$ configuration ($t_{2g}^3e_g^2$, d_{x2-y2}^1, d_{z2}^1, d_{xz}^1, d_{yz}^1, d_{xy}^1). This change of spin-state was accompanied by a significant enhancement in ROS scavenging efficiency, a key property for collagen-induced arthritis (CIA) treatment. Mechanistically, the HS Fe_2-N_6/DAN, endowed with unique interatomic charge-transfer pathways and elevated spin density of the Fe active centers, outperformed the LS Fe-N_4/SAN in three critical antioxidative catalytic activities: hydroxyl radical (•OH) scavenging, superoxide dismutase (SOD)-like activity, and CAT-like activity. Density functional theory (DFT) calculations revealed that Fe-Fe dual-site spin coupling in HS Fe_2-N_6/DAN not only disrupted structural symmetry, enhanced electronic polarization and elevated the population of unpaired electrons in Fe centers but also modulated the Fe 3d orbital electronic structure, thereby accelerating the catalytic reaction kinetics. Furthermore, this Fe–Fe dual-site spin coupling increased the number of unpaired electrons, remodeled the electronic configuration to facilitate interfacial electron transfer, and concomitantly shifted the d-band center of Fe atoms toward the Fermi level (0 eV).

Furthermore, to simultaneously boost the ROS-scavenging capacity of iron-based atomic nanozymes and suppress acid-induced chondrocyte pyroptosis, we introduced a facile acid-base neutralization strategy to achieve synergistic therapeutic effects. We prepared a composite hydrogel using nano-magnesium oxide (nMgO) and gelatin (Gel), and encapsulated two types of iron-based nanozymes separately to construct a pH-responsive enzyme-loaded hydrogel system: nMgO/Gel@Fe-N_4/SAN and nMgO/Gel@Fe_2-N_6/DAN. The *in-situ* acid neutralization mediated by nano-magnesium oxide hydrolysis concurrently inhibits chondrocyte pyroptosis and restores the catalytic activity of Fe-based atomic nanozymes, enabling synergistic antioxidant and anti-inflammatory effects. Both in vitro and in vivo experimental results demonstrated that the composite hydrogel system loaded with HS Fe_2-N_6/DAN (nMgO/Gel@Fe_2-N_6/DAN) effectively reprogrammed the redox microenvironment in the CIA model by virtue of its unique acid-neutralizing capability and spin-state synergistic catalytic effect.

2. Results and discussion

2.1 Preparation and characterization of LS Fe-N_4/SAN and HS Fe_2-N_6/DAN

The synthetic routes for LS Fe-N_4/SAN and HS Fe_2-N_6/DAN are illustrated in Fig. 1. To construct HS Fe_2-N_6/DAN, a two-step protocol is designed using zeolitic imidazolate framework-8 (ZIF) as the template. First, $Fe_2(CO)_9$ are encapsulated in situ within the cages of ZIF-8 to fabricate ZIF@$Fe_2(CO)_9$ precursor. Transmission electron microscopy (TEM) image confirmed that as-synthesized ZIF@$Fe_2(CO)_9$ retains the characteristic rhombic dodecahedral morphology of ZIF (Fig. S1). Subsequent annealing of this precursor at high temperature yielded HS Fe_2-N_6/DAN (Fig. 2a). For LS Fe-N_4/SAN synthesis, $Fe(acac)_3$ was loaded into ZIF-8 (Fig. S2), followed by same pyrolysis process to obtain the final product. High-resolution TEM (HR-TEM) images further revealed that high-temperature pyrolysis renders the surface of both LS Fe-N_4/SAN and HS Fe_2-N_6/DAN rough and porous, a structure favorable for catalytic reactions (Fig. 2b and Fig. S3). Selected area electron diffraction (SAED) of both LS Fe-N_4/SAN and HS Fe_2-N_6/DAN revealed two diffuse rings, which are characteristic of amorphous nitrogen doping carbon (N-C) scaffolds (Fig. 2c and Fig. S4). X-ray diffraction (XRD) patterns of HS Fe_2-N_6/DAN or LS Fe-N_4/SAN show no characteristic peaks corresponding to metallic Fe or Fe oxide nanoparticles (NPs), indicating the absence of Fe-based NPs (Fig. 2d). Energy-dispersive X-ray spectroscopy (EDS)

elemental mapping of HS Fe_2-N_6/DAN displayed bright, uniformly dispersed signals of Fe, confirming the coexistence of atomically dispersed Fe (Fig. 2e-i). Aberration-corrected high-angle annular dark-field scanning transmission electron microscopy (HAADF-STEM) images of HS Fe_2-N_6/DAN clearly visualized numerous isolated bright dots (marked with yellow box and red circles) embedded in the N-C framework-these dots correspond to dual Fe atoms and single Fe atoms (Fig. 2j). Statistical analysis of HS Fe_2-N_6/DAN shows that the distance between two single Fe atoms is 2.0 Å (Fig. 2k), and the inter-atomic distance histogram exhibits a sharp peak at 2.1 Å, confirming the exclusive presence of atomically dispersed Fe (Fig. 2l-m). For LS Fe-N_4/SAN, HAADF-STEM images clearly visualized numerous isolated bright dots (marked with red circles) embedded in the N-C framework-these dots correspond to single Fe atoms (Fig. 2n). And the distance between two single Fe atoms is 2.6 Å (Fig. 2o), with a sharp peak at 2.4 Å in the inter-atomic distance histogram-further verifying the atomic dispersion of Fe (Fig. 2p-q). In addition, Raman analysis demonstrated that two distinct broad peaks situated roughly at 1345 and 1590 cm^{-1} correspond to the D band and G band, respectively (Fig. S5). Collectively, these characterizations confirm the successful fabrication of HS Fe_2-N_6/DAN and LS Fe-N_4/SAN.

X-ray photoelectron spectroscopy (XPS) is employed to investigate the valence states of C and N in HS Fe_2-N_6/DAN. High-resolution C 1s spectrum showed predominant sp^2-hybridized graphitic carbon contributions, including C-C and C-N bonds (Fig. S6). Deconvolution of the N 1s region indicated three nitrogen species: graphitic N, pyridinic N and pyrrolic N. Among these, pyrrolic N served as primary the coordination site that anchor isolated Fe centers, thereby potentiating catalytic performances (Fig. S7). Electron spin resonance (ESR) spectroscopy was also performed on the nanozymes, a technique sensitive to the presence of unpaired electrons. As shown in Fig. 2r, a characteristic signal of high-spin Fe with rhombic zero-field splitting is detected at g = 2.008 (S =3/2), which is more pronounced in HS Fe_2-N_6/DAN compared to LS Fe-N_4/SAN. These results confirmed that Fe-Fe coupling increased the number of unpaired electrons in the Fe center, thereby switching the spin state of single-atom Fe from low spin (in LS Fe-N_4/SAN) to high spin (in Fe_2-N_6/DAN)-a key structural feature underlying the enhanced catalytic activity of HS Fe_2-N_6/DAN.

To further clarify the electronic structure and local coordination environment of Fe atoms in Fe_2-N_6/DAN and LS Fe-N_4/SAN, synchrotron radiation-based X-ray

absorption near-edge structure (XANES) spectroscopy and extended X-ray absorption fine structure (EXAFS) were performed. Fe K-edge XANES spectra showed that the absorption threshold of both Fe_2-N_6/DAN and LS Fe-N_4/SAN between those of Fe foil and Fe_2O_3, confirming the presence of Fe in a partially oxidized state $Fe^{\delta+}$ ($0<\delta<3$) (Fig. 3a). In the Fourier-transformed (FT) EXAFS spectra in R-space exhibited prominent peaks at 1.26 Å (Fe-N) and subordinate peak at 2.3 Å (Fe-Fe), corresponding to the Fe-N and Fe-Fe coordination, in contrast, LS Fe-N_4/SAN showed a peak at 1.41 Å (Fe-N), assigned to the Fe-N coordination (Fig. 3b-g and S8). These results confirmed the atomic dispersion of Fe (no Fe-Fe peaks were observed, ruling out nanoparticle formation) and the difference in local coordination between the two SANs. Quantitative EXAFS fitting analysis further revealed that each Fe center in HS Fe_2-N_6/DAN is coordinated by 3 N atoms and 1 Fe atoms (forming N_3-Fe-Fe-N_3 active sites), while Fe centers in LS Fe-N_4/SAN are coordinated by 4 N atoms (forming Fe-N_4 active sites) (Fig. 3h-j, Fig. S9 and Table S1). Collectively, these characterizations unequivocally confirmed the successful synthesis of HS Fe_2-N_6/DAN and LS Fe-N_4/SAN (Fig. 3k). More importantly, they verified that Fe-Fe coupling modulated both the coordination environment (N_3-Fe-Fe-N_3 vs Fe-N_4) and spin state (high spin vs low spin) of single-atom Fe-two critical structural modifications that contributed to the superior catalytic performance of HS Fe_2-N_6/DAN.

2.2 Preparation, Characterization, and Multi-Enzyme-Mimetic Activities of nMgO/Gel@Fe-N_4/SAN and nMgO/Gel@Fe_2-N_6/DAN

We prepared a nano-magnesium oxide (nMgO) hydrogel material as a carrier for these two nanozymes. Initially, we mixed gelatin powder with nMgO under magnetic stirring. Subsequently, we separately added the pre-synthesized Fe-N_4/SAN or Fe_2-N_6/DAN liquid and continued magnetic stirring until uniformly mixed, thereby obtaining nMgO/Gel@Fe-N_4/SAN or nMgO/Gel@Fe_2-N_6/DAN. Both formulations formed self-supporting hydrogels, as evidenced by the vial-inversion test (Fig. 4a). The gelation time of nMgO/Gel@Fe-N_4/SAN was shorter (≈ 10-11 mins) than that of nMgO/Gel@Fe_2-N_6/DAN (≈ 12-13 mins) (Fig. 4b), indicating faster network formation in the former. SEM images revealed that both hydrogels exhibited a three-dimensional porous architecture with micrometer-scale pores, which is favorable for water retention and mass transport. Elemental mapping (EDS) showed the presence and relatively uniform distribution of Fe, Mg, C, N, and O throughout the hydrogel matrices,

suggesting homogeneous incorporation of the inorganic/organic components and well-constructed networks (Fig. 4c-d).

The C 1s (Fig. 4e) and N 1s (Fig. 4f) XPS spectra of both hydrogels could be deconvoluted into multiple components corresponding to oxygen-/nitrogen-containing functional groups (e.g., C–C/C–H, C–O, C=O/O–C=O and N-related species). Noticeable differences in peak positions and/or relative intensities (marked by dashed lines) were observed between the two samples, implying distinct chemical environments and interaction modes (e.g., coordination and/or hydrogen-bonding/electrostatic interactions), which are consistent with their different network properties. As shown in Fig. 4g-h, both samples exhibit characteristic FTIR bands of O-/N-containing functionalities. The broad band at 3200-3400 cm^{-1} is assigned to -OH/-NH stretching, whereas the weak band at around 2920 cm^{-1} corresponds to C-H stretching. The bands in the 1600-1400 cm^{-1} region can be attributed to the amide I, amide II, and amide III vibrations, indicating the preservation of amide-related organic moieties. More importantly, the amide II band of nMgO/Gel@Fe_2-N_6/DAN shifted from 1534.7 cm^{-1} to 1539.0 cm^{-1} compared to that of nMgO/Gel@Fe-N_4/SAN, confirming the formation of interfacial coordination/chemical coupling between the inorganic single-atom nanozyme and the organic matrix.

The weight loss increased rapidly with degradation time for both hydrogels (Fig. 4i). nMgO/Gel@Fe_2-N_6/DAN exhibited consistently higher weight loss than nMgO/Gel@Fe-N_4/SAN, indicating a faster degradation rate. At ~30 min, nMgO/Gel@Fe_2-N_6/DAN approached ~100% weight loss, whereas nMgO/Gel@Fe-N_4/SAN remained at ~85-90%. Meanwhile, the pH of the degradation medium increased from ~4.8 to approximately 6.3-6.6 over time (Fig. 4j). The pH values for nMgO/Gel@Fe_2-N_6/DAN were slightly higher than those for nMgO/Gel@Fe-N_4/SAN, suggesting a more pronounced or faster influence of degradation/release on the surrounding environment. In the strain sweep (Fig. 4k), both hydrogels showed typical gel-like behavior with G′ > G″ over a broad strain range, confirming stable elastic networks. At higher strain, the moduli decreased, indicating structural breakdown/yielding. Notably, nMgO/Gel@Fe_2-N_6/DAN exhibited a higher overall G′, demonstrating greater stiffness/elastic strength compared with nMgO/Gel@Fe-N_4/SAN. In the temperature sweep (Fig. 4l), both samples displayed a sharp decrease in G′ and G″ around 37-40 °C, suggesting a pronounced temperature-responsive sol–

gel (or gel-sol) transition near physiological temperature. Consistent with the strain sweep, nMgO/Gel@Fe_2-N_6/DAN maintained higher moduli before the transition.

We first assessed the enzymatic activity of the two nanozymes (Fe-N_4/SAN and Fe_2-N_6/DAN) in scavenging •OH or H_2O_2 using electron spin resonance (ESR) spectroscopy. As shown in Fig. 4m, Fe_2-N_6/DAN with a high-spin state exhibited more pronounced •OH scavenging activity, as evidenced by the significantly weakened characteristic •OH pattern (1:2:2:1). Similarly, the high-spin Fe_2-N_6/DAN exhibited superior H_2O_2 scavenging capacity (Fig. 4n), demonstrating that Fe-Fe coupling induced high-spin state of single-atomic Fe substantially enhanced catalytic activity. ESR spectroscopy was further employed to evaluate the $•O_2^-$ scavenging efficiency of the two nanozymes. As demonstrated in Fig. 4o, the HS Fe_2-N_6/DAN displayed more pronounced $•O_2^-$ scavenging activity, with the characteristic signal peaks of $•O_2^-$ being significantly attenuated. The results of the $•O_2^-$ inhibition assay were consistent with the findings described above (Fig. 4p). Collectively, these findings confirmed that that HS Fe_2-N_6/DAN functioned as a robust, broad-spectrum ROS scavenger with exceptional multi-enzymatic activities, positioning it as a promising candidate for RA treatment.

2.3 DFT calculations on the catalytic mechanism of LS Fe-N_4/SAN and HS Fe_2-N_6/DAN

To further elucidate the intrinsic mechanisms underlying the enhanced catalytic activity induced by Fe-Fe coupling, density functional theory (DFT) calculations were performed. The geometrically optimized structures of asymmetric HS Fe_2-N_6/DAN and symmetric LS Fe-N_4/SAN are depicted in Fig. 5a-b. In the LS Fe-N_4/SAN configuration, the Fe center adopted a tetrahedral coordination geometry with surrounding four N atoms. The Fe-N bond lengths exhibited a narrow distribution range, which contributed to reduced charge polarization within the coordination sphere and enhanced symmetry of the Fe atomic orbitals. These structural featured are critical for stabilizing the low-spin state of single-atom Fe in tetrahedral coordination environments typical of Fe-N_4-based single-atom catalysts. Upon the introduction of a second Fe atom, Fe-Fe covalent coordination is formed, inducing distinct modifications to the local bond network of the N-doped carbon support. Specifically, the Fe-N bond length undergoes noticeable elongation, leading to a trigonal coordination mode for each Fe center. This structural rearrangement yielded a thermodynamically stable Fe_2-N_6 binuclear configuration with well-defined Fe coordination environments. In terms of bond length characteristics, the

Fe_2-N_6 structure displayed diminished symmetry relative to Fe-N_4, accompanied by increased charge polarization. This structural distortion elevated the number of unpaired electrons in the Fe 3d orbitals, which significantly enhanced the surface reactivity of the active centers by promoting effective orbital overlap with reactant molecules. Such electronic structure modulation effectively tuned the energy level distribution of Fe 3d orbitals, ultimately boosting the overall catalytic activity of the system.

Hirshfeld charge analysis of Fe centers revealed that the formation of Fe-Fe coupling remarkably enhances the spin density and total magnetic moment of Fe atoms. This electronic structure modulation intensified the charge polarization effect within the entire system and induced distinct spin polarization of Fe centers. Consequently, the electron distribution in Fe d orbitals exhibited a higher degree of asymmetry, which effectively lowered the energy barrier for reactant activation and thus favored the enhancement of system catalytic activity (Fig. 5c-d). Charge density difference (CDD) and Bader charge analyses of asymmetric HS Fe_2-N_6/DAN and symmetric LS Fe-N_4/SAN revealed that following Fe-Fe coupling, HS Fe_2-N_6/DAN exhibited higher charge density during the adsorption of H_2O_2, •OH, and $•O_2^-$. This is accompanied by greater electron transfer between the Fe active centers and reactants, a hallmark of enhanced adsorption strength in single-atom and dual-atom catalysis (Fig. 5e-g). The structures of HS Fe_2-N_6/DAN and LS Fe-N_4/SAN, along with their respective adsorption energies (Eads) for H_2O_2, are illustrated in Fig. 5h. HS Fe_2-N_6/DAN demonstrated stronger H_2O_2 adsorption (more negative Eads values) compared to LS Fe-N_4/SAN, indicating that Fe-Fe coupling optimized the adsorption affinity of the active site for H_2O_2. This improvement is associated with significantly increased electron transfer and elevated charge density at the Fe centers, thereby amplifying the catalytic activity of HS Fe_2-N_6/DAN.

Projected crystal orbital Hamiltonian population (pCOHP) analysis demonstrated that the Fe-O pCOHP value of the HS Fe_2-N_6/DAN structure is relatively lower than that of LS Fe-N_4/SAN. In single-atom catalysis, a lower pCOHP value corresponds to higher bond energy, which strengthened the interaction between Fe centers and oxygen-containing reactants such as H_2O_2 (Fig. S10). Moreover, density of states (DOS) analysis indicated that compared to LS Fe-N_4/SAN, HS Fe_2-N_6/DAN exhibited a continuous increase in electronic states around the Fermi energy level (0 eV). This

feature was highly conducive to electron conduction between the active centers and reactants, thus enhancing the overall electrical conductivity of the catalytic system (Fig. 5i-j). Additionally, the DOS distribution of H_2O_2 adsorbed at the Fe site showed that for the HS Fe_2-N_6/DAN structure, the continuity of electronic states around the Fermi energy level is enhanced, facilitating efficient electron transfer. At the same time, the orbitals of H_2O_2 interact more significantly with Fe 3d orbitals at the Fermi energy level, demonstrating a strengthened adsorption effect and improved efficiency of H_2O_2 activation and transformation (Fig. 5k-l).

DOS analysis of Fe 3d orbitals in HS Fe_2-N_6/DAN, LS Fe-N_4/SAN, H_2O_2-adsorbed HS Fe_2-N_6/DAN, and H_2O_2-adsorbed LS Fe-N_4/SAN showed that the number of d electrons near the Fermi level of the Fe d-band center in HS Fe_2-N_6/DAN is effectively increased. Furthermore, the closer proximity of the d-band center to the Fermi level, consistent with the d-band center theory in heterogeneous catalysis, thus enhancing the adsorption capacity of the system for reactants (Fig. 5m-n and Fig. S11). DOS analysis of Fe 3d orbitals in HS Fe_2-N_6/DAN revealed occupancy of the d_{z2}^1, d_{xz}^1, and d_{yz}^1 orbitals (three unpaired electrons), while LS Fe-N_4/SAN exhibited occupancy of the d_{xz}^2, d_{yz}^2, d_{xy}^2, and d_{x2-y2}^1 orbitals (one unpaired electron) (Fig. 5o). These electronic orbital configurations clearly illustrated the spin-state transition of Fe in nanozymes from low to high spin. In the low-spin state (LS Fe-N_4/SAN), the Fe 3d orbital configuration is (d_{x2-y2}^1, d_{z2}^0, d_{xz}^2, d_{yz}^2, d_{xy}^2), which corresponds to a low magnetic moment (S=1/2). After Fe-Fe coupling (forming HS Fe_2-N_6/DAN), the Fe 3d electronic configuration shifts to (d_{x2-y2}^0, d_{z2}^1, d_{xz}^1, d_{yz}^1, d_{xy}^0), a configuration that defined the high-spin state (S=3/2) and is accompanied by a significantly increased magnetic moment. We proposed that this spin-state transition is primarily driven by Fe-Fe coordination. Fe-Fe coupling weakened the crystal field surrounding Fe and reduced the energy level splitting of Fe 3d orbitals. These effects collectively promoted the conversion of the Fe electronic configuration from paired low-spin to unpaired high-spin, a key electronic modulation strategy in dual-atom catalysis to enhance catalytic activity.

For CAT-like activity, the RDS corresponds to the reduction of adsorbed *OOH + *OH to form adsorbed *OH + *H on the active site. At HS Fe_2-N_6/DAN, this step had an energy barrier of 0.57 eV, which is significantly lower than the 0.64 eV barrier at the Fe-N_4 catalytic site (Fig. 5p and Fig. S12). This demonstrated that the binuclear Fe_2-N_6

active site more effectively promoted the reduction of *OOH + *OH and subsequent O_2 desorption, a critical step in CAT-like catalytic cycles. Similarly, for the conversion of $\bullet O_2^-$ to H_2O_2, the RDS is identified as the desorption of H_2O_2 from the nanozyme surface. Asymmetric HS Fe_2-N_6/DAN exhibited a lower energy barrier for this step (0.11 eV) compared to symmetric LS Fe-N_4/SAN (0.31 eV), indicating that it is more favorable for H_2O_2 desorption and subsequent catalyst reactivation. This is essential for sustaining catalytic cycles in ROS-scavenging applications (Fig. 5q and Fig. S13).

Given that •OH was identified as a ROS generated during catalysis, the •OH scavenging catalytic process can be delineated into six sequential steps: (1) adsorption of •OH onto the catalyst surface (+*OH); (2) reduction of surface-adsorbed 2*OH at catalytic sites to form adsorbed *O and H_2O (*O + H_2O); (3) RDS desorption of H_2O from the catalytic sites (+*O); (4) reduction of adsorbed *O to generate adsorbed *O_2 + H_2O at the catalytic sites (*O_2 + H_2O); (5) desorption of H_2O from the catalytic sites (+*O_2); (6) desorption of *O_2 from the active sites, thereby regenerating the nanozyme. For the RDS (H_2O desorption) at the Fe_2-N_6 active site, the energy barrier was 0.47 eV, which is markedly lower than the 0.64 eV barrier at the Fe-N_4 catalytic site (Fig. 5r and Fig. S14). This lower barrier confirmed that Fe_2-N_6 active sites facilitate H_2O release more readily, accelerating the overall •OH scavenging kinetics. Collectively, these DFT calculation results confirmed that the asymmetric HS Fe_2-N_6/DAN structure constructed via Fe-Fe coupling of symmetric LS Fe-N_4/SAN effectively enhances catalytic activity by synergistically optimizing three key aspects of single-atom and dual-atom catalysis (Fig. 5s). These aspects included the coordination environment and electronic structure of Fe active centers, the adsorption affinity and electron transfer efficiency between Fe centers and reactants, and the energy barriers of rate-determining steps in multi-enzyme-mimetic catalytic cycles.

2.4 nMgO/Gel@Fe_2-N_6/DAN facilitates ROS scavenging and cellular reprogramming of BMDMs under in vitro acidic conditions

A key pathology of RA is synovitis, in which synovial macrophages play a central role. In active RA, pro-inflammatory M1 macrophages abundantly infiltrate the synovium and fuel the inflammatory microenvironment through the secretion of TNF-α, IL-6, and IL-1β. The ROS-rich and acidic microenvironment in RA promotes the polarization of synovial macrophages toward the pro-inflammatory M1 phenotype. Conversely, inducing their polarization toward the anti-inflammatory M2 phenotype is

crucial for inhibiting disease progression. Therefore, evaluating the ROS-scavenging effect of nMgO/Gel@Fe_2-N_6/DAN and its reprogramming effect on macrophage phenotype under acidic conditions in vitro is essential for understanding its protective mechanism in the RA pathological environment. First, biosafety was assessed using bone marrow-derived macrophages (BMDMs) isolated from mice. The results of Calcein-AM and propidium iodide (AM/PI) staining and CCK-8 assay indicated that 20 ppm of Fe-N_4/SAN, nMgO/Gel@Fe-N_4/SAN, Fe_2-N_6/DAN, and nMgO/Gel@Fe_2-N_6/DAN exhibited no cytotoxicity within 12 and 24 hours (Fig. 6a-b and Fig. S15a-b). However, when the concentration of nMgO/Gel@Fe-N_4/SAN or nMgO/Gel@Fe_2-N_6/DAN exceeded 40 ppm, significant cytotoxicity was observed (Fig. S17a-d). Therefore, a concentration of 20 ppm was used for subsequent in vitro BMDMs intervention experiments.

To evaluate the ROS-scavenging effect of nMgO/Gel@Fe_2-N_6/DAN in BMDMs under acidic (pH 4.5) and LPS-stimulated conditions, intracellular ROS levels were measured using the DCFH-DA fluorescent probe. Both CLSM and flow cytometry analyses revealed that Fe-N_4/SAN, nMgO/Gel@Fe-N_4/SAN, Fe_2-N_6/DAN, and nMgO/Gel@Fe_2-N_6/DAN all reduced ROS levels in BMDMs to varying extents. Notably, nMgO/Gel@Fe_2-N_6/DAN-a composite of high-spin Fe_2-N_6/DAN and nano-magnesia alkaline hydrogel—exhibited the most potent ROS-scavenging activity (Fig. 6c-d and Fig S17a-b). These data demonstrate that nMgO/Gel@Fe_2-N_6/DAN effectively attenuates oxidative stress in macrophages under acidic and LPS-stimulated conditions.

Flow cytometry analysis was performed on stimulated BMDMs using CD86 or CD206 antibodies in conjunction with F4/80 antibody. The results showed that exposure to acidic and LPS conditions significantly increased the percentage of F4/80 and CD86 double-positive cells (M1 macrophages), while significantly decreasing the percentage of F4/80 and CD206 double-positive cells (M2 macrophages) (Fig. 6e-h). In contrast, nMgO/Gel@Fe_2-N_6/DAN treatment markedly promoted the polarization of BMDMs toward the M2 phenotype (Fig. 6e-h). Furthermore, Western blot and qRT-PCR analyses demonstrated that nMgO/Gel@Fe_2-N_6/DAN significantly downregulated the expression levels of M1 macrophage markers (NOS2 and CD86), IL-1β, and TNF-α (Fig. 6i-l and Fig. S18a), while significantly upregulating the expression levels of M2 macrophage markers [CD206, arginase-1 (Arg-1), IL-4, and

IL-10] (Fig. 6i,m-o and Fig. S18b). These data indicate that nMgO/Gel@Fe_2-N_6/DAN promotes the polarization of macrophages from M1 to M2 phenotype under acidic and LPS-stimulated conditions.

2.5 nMgO/Gel@Fe_2-N_6/DAN promotes ROS scavenging and inhibits pyroptosis in chondrocytes under acidic conditions in vitro

Articular cartilage, which together with the synovium forms the joint barrier, is another key pathological feature of RA, and its destruction is often accompanied by chondrocyte pyroptosis. Studies have shown that the acidic microenvironment in RA can activate acid-sensing ion channel 1a (ASIC-1a) on the surface of chondrocytes, inducing substantial ROS generation and subsequently triggering chondrocyte pyroptosis. Therefore, evaluating the ROS-scavenging capacity of nMgO/Gel@Fe_2-N_6/DAN in chondrocytes in vitro is of great significance for elucidating its inhibitory effect on pyroptosis.

In this study, primary murine chondrocytes were first used as an in vitro model to evaluate the biocompatibility of the materials. Similar to the results observed in BMDMs, treatment with 20 ppm of each material for 12 h and 24 h did not induce significant cytotoxicity in chondrocytes (Fig. 7a-b and Fig. S19 a-b). AM/PI staining further confirmed that when the concentration was increased to 40 ppm or higher, nMgO/Gel@Fe-N_4/SAN and nMgO/Gel@Fe_2-N_6/DAN exhibited significant cytotoxic effects (Fig. S20a-d). Accordingly, 20 ppm was selected as the intervention concentration for subsequent experiments. Functional assessment revealed that under acidic and LPS-stimulated conditions, nMgO/Gel@Fe_2-N_6/DAN exhibited the most pronounced ROS-scavenging effect in chondrocytes (Fig 7c-d and Fig. S21a-b).

We further evaluated the effect of nMgO/Gel@Fe_2-N_6/DAN on chondrocyte pyroptosis under acidic and LPS-stimulated conditions in vitro. The results showed that exposure to acidic and LPS conditions significantly increased the percentage of $PI^+Caspase\text{-}1^+$ double-positive (cells in pyroptosis) cells (Fig. 7e-f). While all material interventions reduced the pyroptosis rate to varying degrees, nMgO/Gel@Fe_2-N_6/DAN exhibited the most pronounced reduction, attributed to the synergistic effect of its high-spin state and acidity-neutralizing capacity (Fig. 7e-f). Pyroptosis is accompanied by the release of pro-inflammatory cytokines such as IL-1β and IL-18, and the nMgO/Gel@Fe_2-N_6/DAN group likewise showed the most significant downregulation

of these factors (Fig. 7g-h and Fig. S22a-b).

2.6 nMgO/Gel@Fe_2-N_6/DAN attenuates synovitis, chondrocyte pyroptosis, and bone destruction in CIA mice

We further evaluated the therapeutic efficacy of nMgO/Gel@Fe_2-N_6/DAN in a CIA mouse model, a widely adopted model due to its high similarity to human RA in terms of pathogenesis and pathological features. At 21 days post-immunization, the arthritic mice were randomly divided into five groups and received weekly intra-articular injections of PBS, nMgO/Gel, Fe_2-N_6/DAN, nMgO/Gel@Fe_2-N_6/DAN, or methotrexate (MTX) into the knee and ankle joints. The treatment lasted until day 60, after which the mice were euthanized, and joint tissues along with major organs were collected for subsequent analysis (Fig. 8a). MTX, a first-line clinical drug for RA, was used as a positive control, while normal mice served as a negative control. The results showed that both nMgO/Gel@Fe_2-N_6/DAN and MTX treatment significantly reduced paw thickness and knee joint diameter in the model mice (Fig. 8b-d). Assessment of locomotor activity via the open field test revealed that nMgO/Gel@Fe_2-N_6/DAN markedly improved motor function in arthritic mice (Fig. 8e-f). Histological staining was further performed to evaluate the extent of synovial inflammation, chondrocyte pyroptosis, and bone destruction. H&E staining demonstrated that nMgO/Gel@Fe_2-N_6/DAN significantly alleviated synovial inflammation (Fig. 9a-d). Subsequently, immunofluorescence co-localization of F4/80 with CD86 or CD206 was conducted to assess macrophage subset distribution in the synovium. Consistent with the in vitro results, nMgO/Gel@Fe_2-N_6/DAN significantly promoted the phenotypic switch of synovial macrophages from M1 to M2 (Fig. 9e-h and Fig. S23a-d).

Safranin-O/Fast Green staining of articular cartilage revealed severe cartilage collapse and destruction in the PBS and nMgO/Gel groups, with Mankin scores significantly higher than those in the normal group. In contrast, the nMgO/Gel@Fe_2-N_6/DAN and MTX groups exhibited relatively intact cartilage morphology and significantly lower Mankin scores (Fig. 10a, b, g, i), indicating that nMgO/Gel@Fe_2-N_6/DAN effectively alleviates articular cartilage damage. Based on our in vitro finding that nMgO/Gel@Fe_2-N_6/DAN inhibits chondrocyte pyroptosis, we further examined the expression of NLRP3 and GSDMD in articular cartilage by immunofluorescence in vivo. Although Fe_2-N_6/DAN, nMgO/Gel@Fe_2-N_6/DAN, and MTX all reduced the levels of these pyroptosis markers to varying extents (Fig. 10c, d, h, j and Fig. S24a-d),

nMgO/Gel@Fe_2-N_6/DAN exhibited the most pronounced effect. These findings suggest that targeting the acidic microenvironment in RA to alleviate chondrocyte pyroptosis represents an effective therapeutic strategy. Bone erosion is a characteristic pathological manifestation of advanced RA. Micro-CT analysis revealed that nMgO/Gel@Fe_2-N_6/DAN treatment significantly ameliorated severe bone destruction in the knee and ankle joints (Fig. 10e-f). Quantitative analysis of bone parameters further demonstrated that nMgO/Gel@Fe_2-N_6/DAN significantly increased bone volume per tissue volume (BV/TV) (Fig. 8k, m) and trabecular number (Tb.N mm^{-1}) (Fig. 8l, n). Collectively, these results indicate that nMgO/Gel@Fe_2-N_6/DAN effectively alleviates synovial inflammation, chondrocyte pyroptosis, and bone erosion in arthritic mice. To evaluate its in vivo biosafety, we measured serum biomarkers of liver and kidney function and performed H&E staining of major organs. The results showed that serum levels of ALT, AST, BUN, and Cre in the nMgO/Gel@Fe_2-N_6/DAN group were comparable to those in the normal group (Fig. S25a), and no significant pathological changes were observed in major organs (Fig. S25b).

2.7 Functional mechanism of nMgO/Gel@Fe_2-N_6/DAN in promoting macrophage polarization toward an anti-inflammatory phenotype and inhibiting chondrocyte pyroptosis

To investigate the mechanism by which nMgO/Gel@Fe_2-N_6/DAN promotes anti-inflammatory polarization of macrophages, BMDMs were cultured under acidic and LPS-stimulated conditions and treated with either PBS or nMgO/Gel@Fe_2-N_6/DAN, followed by bulk RNA sequencing analysis. The results revealed a total of 2,159 differentially expressed genes (DEGs) between the two groups, of which 1,431 were upregulated and 728 were downregulated (Fig. S26a-c). Gene Ontology (GO) analysis showed that the differentially expressed genes were significantly enriched in several biological processes associated with RA progression, such as inflammatory response, regulation of immune response, response to oxidative stress, reactive oxygen species metabolic process, and positive regulation of NF-κB transcription factor activity. Meanwhile, significant enrichment was also observed in molecular functions such as oxidoreductase activity, antioxidant activity, and glutathione peroxidase activity (Fig. 11a and Fig. S27a). Cluster analysis revealed that the key antioxidant enzyme gene *Glutathione Peroxidase 4 (GPX4)* was significantly upregulated in the nMgO/Gel@Fe_2-N_6/DAN group, whereas the pro-oxidase gene *NADPH Oxidase 3*

(NOX3) was downregulated. This regulatory trend was confirmed by qRT-PCR validation (Fig. 11b and Fig. S28a-b). Pathway enrichment analysis using the Kyoto Encyclopedia of Genes and Genomes (KEGG) revealed that the differentially expressed genes were significantly enriched in inflammation- and bone metabolism-related signaling pathways, including osteoclast differentiation, rheumatoid arthritis, TNF signaling pathway, NF-κB signaling pathway, and IL-17 signaling pathway (Fig. S27b). Furthermore, nMgO/Gel@Fe_2-N_6/DAN treatment downregulated the expression of pro-inflammatory factors (*MMP9, IL-1β, IL-6, NOS2*) and bone resorption markers (*Acp5, Ctsk*) in BMDMs, while upregulating anti-inflammatory genes (*Arg1, IL-10rb*) (Fig. 11b). These molecular alterations were consistent with the observed in vivo phenotypes of attenuated synovial inflammation and suppressed bone erosion in CIA mice. Additionally, TRAP staining and qRT-PCR analysis demonstrated that the supernatant from nMgO/Gel@Fe_2-N_6/DAN-treated BMDMs effectively inhibited osteoclast activity and the expression of osteoclast-related genes (Fig. S29a-e).

Both GO and KEGG analyses suggested that the NF-κB signaling pathway may play a critical role in nMgO/Gel@Fe_2-N_6/DAN -mediated regulation of macrophage phenotype. Given that activation of the NF-κB pathway is closely associated with intracellular ROS levels, we further examined the expression of related proteins. Western Blot results showed that nMgO/Gel@Fe_2-N_6/DAN treatment significantly reduced the protein level of phosphorylated NF-κB (p-NF-κB) (Fig. S30a-b). Gene set enrichment analysis (GSEA) further confirmed that both the rheumatoid arthritis signaling pathway and the NF-κB signaling pathway were significantly suppressed in the treatment group (Fig. S31a-b). Collectively, these results demonstrate that nMgO/Gel@Fe_2-N_6/DAN regulates the inflammatory phenotype of macrophages by inhibiting NF-κB phosphorylation.

To investigate the mechanism by whichnMgO/Gel@Fe_2-N_6/DAN alleviates chondrocyte pyroptosis, treated chondrocytes were subjected to bulk RNA sequencing analysis. The results revealed a total of 1,796 differentially expressed genes (DEGs) between the two groups, comprising 1,140 upregulated and 656 downregulated genes (Fig. S32a-c). GO analysis showed that the identified genes were primarily involved in various biological processes related to inflammation, cartilage development, and oxidative stress, including inflammatory response, regulation of inflammatory response, cartilage development, response to oxidative stress, canonical NF-κB signal

transduction, and cellular response to oxidative stress (Fig. 11c). Cluster analysis revealed that, similar to its effect in macrophages, nMgO/Gel@Fe_2-N_6/DAN upregulated *GPX4* and downregulated *NOX3*, a finding confirmed by qRT-PCR (Fig. 11d-f). More importantly, we observed that multiple key pyroptosis-related genes, including *Gsdmd*, *Casp1*, and *Nlrp3*, were downregulated following nMgO/Gel@Fe_2-N_6/DAN treatment, consistent with the inhibition of pyroptosis observed both in vitro and in vivo (Fig. 11d).

Recent studies have revealed that the NF-κB signaling pathway plays a critical role in acidic microenvironment-induced chondrocyte pyroptosis in RA. In the present study, both KEGG (Fig. S33a) and GSEA (Fig. S34a-b) enrichment analyses demonstrated that the NF-κB signaling pathway was significantly suppressed following nMgO/Gel@Fe_2-N_6/DAN treatment. Moreover, this treatment downregulated key genes within the pathway, including *Rela*, *Relb*, *Nfkb1*, and *Nfkb2* (Fig. 11d). Western blotting further confirmed that nMgO/Gel@Fe_2-N_6/DAN treatment markedly reduced the level of phosphorylated NF-κB (p-NF-κB) in chondrocytes (Fig. S35a-b). Collectively, these findings indicate that nMgO/Gel@Fe_2-N_6/DAN alleviates chondrocyte pyroptosis in RA through effective inhibition of the NF-κB signaling pathway.

3. Conclusion

In summary, we report a triadic design paradigm of 'redox-regulated nanoarchitectures-electronic modulation-biological function' for RA therapy by engineering HS Fe_2-N_6/DAN encapsulated in pH-responsive nMgO/Gel hydrogels. Through rational selection of binuclear Fe precursors, we successfully constructed atomically dispersed Fe_2-N_6 configurations with a HS $t_{2g}^3e_g^2$ electronic state, which outperforms LS Fe-N_4/SAN in ROS-scavenging activities. Structural characterizations and DFT calculations collectively reveal that Fe-Fe dual-site coupling breaks the symmetry of the coordination environment, elevates spin density, optimizes d-band center distribution, and reduces the activation energy barriers of rate-determining steps catalytic limitations of conventional SANs. The integration of Fe_2-N_6/DAN into nMgO/Gel hydrogels achieves dual synergistic effects: nMgO-mediated acid neutralization mitigates the RA acidic microenvironment-induced catalytic inactivation and chondrocyte pyroptosis, while the HS Fe_2-N_6/DANs efficiently scavenge excessive ROS. In vitro experiments confirm that this composite system reprograms pro-

inflammatory M1 macrophages toward the reparative M2 phenotype and suppresses chondrocyte pyroptosis by inhibiting the NF-κB signaling pathway. In vivo studies on CIA mice further validate its therapeutic efficacy, as evidenced by attenuated synovial inflammation, preserved cartilage integrity, ameliorated bone erosion, and restored locomotor function, comparable to or exceeding the clinical drug MTX without detectable systemic toxicity. This work pioneers spin-state engineering as a powerful strategy to tune the catalytic activity of Fe-based nanozymes, providing new insights into the structure-activity relationship of dual-atom catalysts. The pH-responsive composite hydrogel design addresses the critical challenge of nanozyme delivery and function in pathological microenvironments. Beyond RA therapy, this versatile framework offers a blueprint for developing next-generation spin-dependent nanozymes to treat ROS-driven degenerative diseases, bridging the gap between electronic structure modulation and translational biomedical applications.

4. Materials and methods

Materials

Gelatin from porcine skin (Gel) and nano magnesium oxide (nMgO; 5-100 nm) were obtained from Sigma-Aldrich Co. (Shanghai, China). DCFH-DA probe was brought from Beyotime (Shanghai, China). Antibodies against NOS2, IL-1β, IL-10, Arg-1, Caspase-1, NLRP3, GSDMD-N, NF-κB, and pNF-κB for Western blot were purchased from Proteintech (Chicago, USA). Antibodies against F4/80, CD86, CD206, and GSDMD for immunofluorescence staining were purchased from Proteintech (Chicago, USA). Antibodies against NLRP3 for immunofluorescence staining were purchased from ABclonal Technology (Wuhan, China).

Synthesis of LS Fe-N_4/SAN and HS Fe_2-N_6/DAN

To synthesize LS Fe-N_4/SAN, 4 g of 2-methylimidazole and 100 mg of $Fe(acac)_3$ were dissolved in 100 mL of methanol in a 250 mL flask to form solution A. A separate solution, designated as solution B, was prepared by dissolving 2 g of $Zn(NO_3)_2$•$6H_2O$ in 80 mL of methanol. Subsequently, solution A was combined with solution B, and the mixture was stirred continuously for 12 hours. The resultant ZIF-8@Fe powders were isolated via centrifugation, followed by multiple washes with methanol and overnight drying in a vacuum oven at 65 °C. The LS Fe-N_4/SAN material was ultimately synthesized through a one-step pyrolysis approach. The ZIF@Fe powder was placed in

a tubular furnace and pyrolyzed at 950 °C for 3 hours under an argon atmosphere.

For the synthesis of HS Fe_2-N_6/DAN, 4 g of 2-methylimidazole, 80 mg of $Fe_2(CO)_9$ were dissolved in 100 mL of methanol in a 250 mL flask to form solution A. Separately, 2 g of $Zn(NO_3)_2$•$6H_2O$ was dissolved in 80 mL of methanol to form solution B. Solution A was then mixed with solution B, and the resulting mixture was stirred for 12 hours. The ZIF-8@$Fe_2(CO)_9$ powders were subsequently collected by centrifugation, washed several times with methanol, and dried at 55 °C in a vacuum oven overnight. The HS Fe_2-N_6/DAN was obtained by a one-step pyrolysis strategy. The ZIF-8@$Fe_2(CO)_9$ powder was placed in a tubular furnace and pyrolyzed at 950 °C for 3 hours under an argon atmosphere.

Preparation of nMgO/Gel@Fe-N_4/SAN and nMgO/Gel@Fe_2-N_6/DAN hydrogels

Gel powder was immersed in deionized water for 2 h to swell and stirred with a magnetic stirrer at 25 °C for 30 min to form a homogeneous solution of 10% (w/v). Then, the obtained Gel was accurately premixed with Nano magnesium oxide (nMgO; 5-100 nm) from Sigma-Aldrich Co. (Shanghai, China) to obtain homogeneous nMgO/Gel hydrogels. Later, the nMgO/Gel was separately mixed with Fe-N_4/SAN and Fe_2-N_6/DAN solutions at a volume ratio of 1:80 to obtain composites (named as nMgO/Gel@Fe-N_4/SAN and nMgO/Gel@Fe_2-N_6/DAN).

Characterization of hydrogels

The gelation time of hydrogels was determined using the vial tilting method, as referred to the previous reference. After freeze-drying, the surface morphology of samples was investigated by scanning electron microscope with an energy dispersive spectrometer (SEM/EDS, Apreo S, USA) at an accelerating voltage of 20 kV. The interaction of nMgO/Gel hydrogel with Fe/SAN and Fe_2/DAE was performed using X-ray photoelectron spectroscopy (XPS, AXIS Supra, Japan). The specific chemical groups of hydrogels were analyzed by FTIR spectroscopy. Data was acquired in the range of 4000-400 cm^{-1} at a spectral resolution of 4 cm^{-1} for 32 scans.

For evaluation of degradation, the nMgO/Gel@Fe-N_4/SAN and nMgO/Gel@Fe_2-N_6/DAN hydrogels with a size of ϕ7×6 mm was soaked in phosphate buffer solution. The pH values of hydrogels were determined using a pH meter (PHS-3C, Shanghai instrument electric science instrument Co. Ltd., China) at 10, 20, 30, and 40 min, respectively. At each test time point, the hydrogels were weighed immediately on

electronic scale.

Rheological characterization of hydrogels was performed on an AR 2000 rheometer (TA Instruments) with parallel plates 20 mm in diameter with a 1 mm gap to confirm basic viscoelasticity and yield strength. The stress and strain gradient changes of the samples were first measured to determine the linear viscoelastic region of the materials. In the linear viscoelastic region, the oscillatory shear tests were conducted on the hydrogels at a constant oscillatory frequency of 1 Hz, 1% strain, and 25 °C.

Investigation of antioxidant performance of Fe_2-N_6/DAN

To detect •OH, ESR spectroscopy was employed, utilizing 5,5-dimethyl-1-pyrroline-N-oxide (DMPO) as a spin-trapping agent for the short-lived radicals. A reaction mixture containing 2 mM H_2O_2, 10 μM $FeSO_4$, 1.5 mM DMPO, and either Fe-N_4/SAN or Fe_2-N_6/DAN was prepared in PBS. Subsequently, an aliquot of 100 μL of this mixed solution was analyzed by ESR. To assess O_2•$^-$ scavenging activity, a mixture containing 1 mM xanthine, 0.2 U/mL XO, 5 mM DMPO, and either Fe-N_4/SAN or Fe_2-N_6/DAN was prepared in PBS. An aliquot of 100 μL of this solution was then transferred to a quartz tube for ESR analysis.

Animals and collagen-induced arthritis (CIA) model

Male DBA/1J mice, 7–8 weeks old, were purchased from GemPharmatech (Jiangsu, China), and kept in a clean and sterile environment with free access to food and water.

According to a prior study, we established the CIA mice model. To induce CIA, an emulsion was prepared by combining bovine type II collagen (2 mg/mL, Chondrex) dissolved in acetic acid with an equal volume of Complete Freund's adjuvant (CFA, Chondrex). The mixture was emulsified continuously for 30 minutes using a handheld homogenizer maintained in an ice bath. On day 0 and day 21, each mouse received a 0.1 mL subcutaneous injection of the emulsion at the tail base. Arthritis development was assessed every three days throughout the experiment. Male DBA/1J mice were assigned to six experimental groups: normal, PBS, nMgO/Gel, Fe_2-N_6/DAN (20 ppm), nMgO/Gel@Fe_2-N_6/DAN (20 ppm), and methotrexate (MTX, 0.5 μg/μL) groups. After successful induction of CIA, the animals received weekly intra-articular injections of the respective treatments (10 μL per injection) into both knee and ankle joints for six consecutive weeks. Sixty days following the initial immunization, all mice were humanely euthanized, and knee joint samples were harvested for micro-computed

tomography (micro-CT) imaging and further histopathological analysis.

Cell viability test

Cell viability was assessed by utilizing the Cell Counting Kit-8 (C0038, Beyotime Biotechnology). Following a 12 or 24-h incubation of BMDMs or chondrocytes with Fe-N_4/SAN, nMgO/Gel@Fe-N_4/SAN, Fe_2-N_6/DAN, and nMgO/Gel@Fe_2-N_6/DAN, the CCK-8 assay was carried out following the guidelines provided by the manufacturer.

Investigation of M2 repolarization induction efficacy of nMgO/Gel@Fe_2-N_6/DAN in vitro

To assess the M2-polarizing potential of nMgO/Gel@Fe_2-N_6/DAN, bone marrow-derived macrophages (BMDMs) were utilized. BMDMs were obtained from 8-week-old healthy DBA/1J mice euthanized via cervical dislocation. Following dissection of the femur and tibia, bone marrow was flushed out and mononuclear cells were isolated after erythrocyte lysis. The isolated cells were seeded into 6-well plates and maintained in culture for 7 days. Each well contained 3 mL of complete medium supplemented with M-CSF at a final concentration of 10 ng/mL. After 24 hours of stimulation with LPS, the BMDMs were exposed to various compounds (Fe-N_4/SAN, nMgO/Gel@Fe-N_4/SAN, Fe_2-N_6/DAN, or nMgO/Gel@Fe_2-N_6/DAN) for an additional 24 hours under acidic conditions (pH ≈ 4.5). Finally, BMDMs were washed and collected for staining of antibodies (PE-F4/80, APC-CD86, FITC-CD206). After being subjected to flow cytometry analysis, the $F4/80^+CD86^+$ or $F4/80^+CD206^+$ cell percent were obtained by Flowjo software.

Investigation of the efficacy of nMgO/Gel@Fe_2-N_6/DAN in inhibiting chondrocytes pyroptosis in vitro

To evaluate the ability of nMgO/Gel@Fe_2-N_6/DAN to inhibit chondrocyte pyroptosis in vitro, mouse primary articular chondrocytes were used. Chondrocytes were obtained from 8-week-old healthy DBA/1J mice euthanized via cervical dislocation. Briefly, cartilage from the femur and knee joint was dissected using a scalpel and digested with 0.25% trypsin in an incubator for 30 minutes. The digestion was then terminated by adding DMEM high-glucose medium supplemented with 5% serum. After discarding the medium, a mixture of 0.15% hyaluronidase and 0.4% type II collagenase (1:1 volume ratio) was added to continue digestion for 14-18 hours. Finally, the cells were filtered through a 70 μm cell strainer to obtain chondrocytes, which were subsequently

seeded into 6-well culture plate. After 24 hours of stimulation with LPS, the chondrocytes were exposed to various compounds (Fe-N_4/SAN, nMgO/Gel@Fe-N_4/SAN, Fe_2-N_6/DAN, or nMgO/Gel@Fe_2-N_6/DAN) for an additional 24 hours under acidic conditions (pH ≈ 4.5). Finally, chondrocytes were washed and collected for staining of antibodies (PI and Caspase-1). After being subjected to flow cytometry analysis, the PI^+ Caspase-1^+ cell percent were obtained by Flowjo software.

Examination of ROS scavenging efficacy in BMDMs and chondrocytes

The ROS was determined by fluorescence microscopy and flow cytometry. The BMDMs or chondrocytes were seeded in a 6-well culture plate overnight. After incubated with LPS for 24 h, BMDMs or chondrocytes were treated with different agents under acidic conditions (pH≈4.5) for another 24 h. Then, cell culture medium was removed and incubated with DCFH-DA solution (S0033S, Beyotime) for at 37°C for 30 min. After being washed for 3 times with PBS, the culture dishes were observed with a confocal fluorescence microscope (Olympus). The ROS level was also quantified by flow cytometry. After incubating for 30 min, the cell dishes were washed for 3 times and then detached by trypsin and analyzed by flow cytometry (BeckMan CytoFLEX).

qRT-PCR and western blot analysis

Total RNA and proteins were extracted from treated BMDMs and chondrocytes using Trizol (Thermo Fisher) and cell lysis buffer (Cell Signaling Technology), respectively, following the manufacturer's protocols. Single-stranded complementary DNA (cDNA) was synthesized using TransScript Uni All-in-One First-Strand cDNA Synthesis SuperMix (TransGen, China), and qRT-PCR was performed using PerfectStart Green qPCR SuperMix (TransGen, China) and StepOnePlus Real-Time PCR System (Applied Biosystems). mRNA expression levels were normalized to GAPDH. The primer sequences are available in Table S2.

For Western blot analysis, a bicinchoninic acid (BCA) kit (TherMo Fisher Scientific) was carried out for measurement of protein concentration. Equal amounts of protein samples (30-50 μg) were separated on 8-12% SDS-PAGE and transferred onto PVDF membranes. Membranes were blocked with 5% BSA for 1 hour, followed by overnight incubation at 4°C with specific primary antibodies. After three washes with TBST, the membranes were incubated with corresponding HRP-labeled secondary

antibodies at room temperature for 1 hour. After another three washes with TBST, the target proteins were visualized using an enhanced chemiluminescence kit. Grayscale analysis was performed using Image J software. GAPDH (1:50000, Proteintech) served as a normalizer. All experiments were independently repeated three times to ensure reliability. The following antibodies were used: NOS2 (1:1000, Proteintech), CD86 (1:1000, Proteintech), IL-1β (1:1000, Proteintech), IL-10 (1:1000, Proteintech), CD206 (1:1000, Proteintech), Arg-1 (1:1000, Proteintech), Caspase-1 (1:1000, Proteintech), NLRP3 (1:1000, Proteintech), GSDMD-N (1:2000, MCE), NF-κB (1:5000, Proteintech) and pNF-κB (1:1000, Proteintech).

Open-field test

Based on the experimental design, complete the numbering and grouping of mice, and prepare the open field apparatus, camera, and related equipment. Before the experiment, allow the animals to acclimate to the test environment for 2 hours. Thoroughly clean the open field apparatus and empty cages with alcohol, and replace the bedding. Debug the software and camera equipment to ensure proper operation. During the experiment, set a 5-second delay for recording, gently place the mouse in the center of the open field apparatus, and allow the system to automatically track and record its movement trajectory for 30 minutes. Each mouse undergoes the experiment 3 times, with total distance recorded to assess motor function.

Immunofluorescence staining

After euthanasia, mice were perfused with 50 mL of 4% PFA. Intact knee joint tissues were harvested and fixed in 4% PFA for 1 day, followed by dehydration in 30% sucrose. The tissues were embedded, sectioned sagittal (30 μm) using a cryostat, and blocked in PBS containing 0.3% Triton and 5% bovine serum albumin (BSA) at room temperature for 2 hours. The sections were then incubated overnight at 4°C with the following primary antibodies: F4/80 (1:200, Proteintech), CD86 (1:100, Proteintech), CD206 (1:100, Proteintech), NLRP3 (1:200, ABclonal Technology) and GSDMD (1:100, Proteintech). After washing, sections were incubated with secondary antibodies at room temperature for 2 hours. Cell nuclei were counterstained with mounting medium containing DAPI (Abcam, ab104139, 1:1000). Fluorescence images were acquired using a laser confocal microscope (Zeiss).

Histopathological examination

The knee joint samples were collected and fixed in 4% paraformaldehyde, then decalcified in a 15% ethylenediaminetetraacetic acid tetrasodium solution for one month. Following paraffin embedding, 3 μm-thick sections were obtained and subjected to hematoxylin-eosin (H&E) and Safranin-O Fast Green staining. Observation and imaging of the stained sections were performed under a light microscope (Olympus).

Micro-CT imaging

Before conducting histological analysis, the preserved joint samples underwent scanning with a micro-CT (NEMO, NMC-200) at a resolution of 19 μm, 90-KV voltage, 90-μA current, and 300-ms exposure time. Subsequently, the obtained micro-CT images were examined with Avatar software.

Safety assessment in vivo

To evaluate the biocompatibility of different nanoparticles, blood serum was collected from mice post-administration. The concentrations of aspartate aminotransferase (AST), alanine aminotransferase (ALT), blood urea nitrogen (BUN), and creatinine (Cre) were measured employing commercial assay kits, following the protocols provided by the manufacturer.

RNA sequencing and analysis

BMDMs or chondrocytes were exposed to nMgO/Gel@Fe_2-N_6/DAN under acidic conditions and LPS stimulation, followed by total RNA extraction using Trizol. PBS-treated BMDMs or chondrocytes served as the control group. The RNA library for RNA-seq was prepared as follows: mRNA was purified from total RNA using poly T and then fragmented into 300-350 bp fragments. The first strand cDNA was reverse transcribed using fragmented RNA and dNTPs, and second-strand cDNA synthesis was subsequently performed. Remaining overhangs of double-strand cDNA were converted into blunt ends via exonuclease/polymerase activities. After adenylation of 3' ends of DNA fragments, sequencing adaptors were ligated to the cDNA, and the library fragments were purified. The template was enriched by PCR, and the PCR product was purified to obtain the final library. After library construction, the concentration of the library was measured by the Qubit® fluorometer. The accurate concentration of the cDNA library was again examined using qPCR. The size distribution of the library was detected by agarose gel electrophoresis. After library preparation and pooling of different samples, the samples were subjected to Illumina NovaSeq sequencing. For

subsequent GO analysis, differentially expressed genes were analyzed in the GO database (http://www.geneontology.org/). Genes were considered differentially expressed when the adjusted P value was lower than 0.05. The list of differentially expressed genes was used in pathway enrichment analysis. In organisms, different genes coordinate to perform their biological functions. Pathway-based analysis helps to further understand the biological functions of genes. KEGG is the main public database for Pathways. Pathway significance enrichment analysis uses KEGG Pathway as the unit and applies hypergeometric testing to find Pathways that are significantly enriched in differentially expressed genes compared to background genes. Gene ontology (GO) terms in the Biological Processes category with $P < 0.05$ were considered significant.

Statistical analysis

Data analysis was performed with GraphPad Prism, Origin, VASP, Avantage, and Image J software, while IVIS was utilized for in vivo imaging processing. Results from at least three independent replicates are expressed as mean ± standard deviation (SD). Details regarding sample size (n), normalization methods, and the specific statistical tests applied are provided in the respective figure legends. For group comparisons, either one-way ANOVA with a Tukey post-hoc test were employed, with a two-sided p-value < 0.05 deemed statistically significant. (represented as $*p < 0.05$, $**p < 0.01$, $***p < 0.001$, or not significant (ns)).

Data availability statement

The main data supporting the results of this study are available within the paper and its Supplementary Information. Any other raw data or noncommercial material used in this study are available from the corresponding author. Source data are provided with this paper.

Author contributions statement

Y. Z. and X. Y. F. conceived and designed the experiments; L. L., Y. T. L. and H. C. contributed equally to this work; J. X. H., H. Y. L., H. X. W., and P. H. W. analyzed the data and drew the figures; H. J. Z. and H. C. contributed to experiments; W. M. Z. reviewed the manuscript; all authors reviewed and approved the final manuscript.

Funding

This work was supported by: National Natural Science Foundation of China (32501233,

82571554), Joint Funds for the Innovation of Science and Technology, Fujian Province (2025Y9246), Natural Science Foundation of Fujian Province (2026J009051, 2025J01087), Fujian Provincial Health Technology Project (2024CXA017).

Declarations

Animal experiments were performed according to the protocol approved by The Ethical Committee (IACUC FJMU 2022-NSFC-0368).

Conflict of Interest

The authors declare no conflict of interest.

Reference

1. Finckh, A. *et al.* Global epidemiology of rheumatoid arthritis. *Nat. Rev. Rheumatol.* **18**, 591-602 (2022).
2. Zhang, F. *et al.* Deconstruction of rheumatoid arthritis synovium defines inflammatory subtypes. *Nature* **623**, 616-624 (2023).
3. Alivernini, S., Firestein, G.S. & McInnes, I.B. The pathogenesis of rheumatoid arthritis. *Immunity* **55**, 2255-2270 (2022).
4. Konzett, V. & Aletaha, D. Management strategies in rheumatoid arthritis. *Nat Rev Rheumatol.* **20**, 760-769 (2024).
5. Kurowska-Stolarska, M. & Alivernini, S. Synovial tissue macrophages in joint homeostasis, rheumatoid arthritis and disease remission. *Nat. Rev. Rheumatol.* **18**, 384-397 (2022).
6. Cutolo, M., Soldano, S., Smith, V., Gotelli, E. & Hysa, E. Dynamic macrophage phenotypes in autoimmune and inflammatory rheumatic diseases. *Nat Rev Rheumatol.* **21**, 546-565 (2025).
7. Li, Z. *et al.* Bioengineered photosynthetic nanothylakoids reshape the inflammatory microenvironment for rheumatoid arthritis therapy. *Nat. Nanotechnol.* **21**, 125-139 (2026).
8. Zhao, K. *et al.* Acid-sensing ion channels regulate nucleus pulposus cell inflammation and pyroptosis via the NLRP3 inflammasome in intervertebral disc degeneration. *Cell Prolif.* **54**, e12941 (2021).
9. Ji, S. *et al.* Matching the kinetics of natural enzymes with a single-atom iron nanozyme. *Nat. Catal.* **4**, 407-417 (2021).
10. Wang, D. *et al.* Self-assembled single-atom nanozyme for enhanced photodynamic therapy treatment of tumor. *Nat. Commun.* **11**, 357 (2020).
11. Huang, L., Chen, J., Gan, L., Wang, J. & Dong, S. Single-atom nanozymes. *Sci. Adv.* **5**, eaav5490 (2019).
12. Zhang, Y. *et al.* Nanozymes for nanohealthcare. *Nat. Rev. Methods Primers* **4**, 36 (2024).
13. Zhang, S. *et al.* Single-atom nanozymes catalytically surpassing naturally

occurring enzymes as sustained stitching for brain trauma. *Nat. Commun.* **13**, 4744 (2022).
14. Zhu, Y. *et al.* Stimuli-Responsive Manganese Single-Atom Nanozyme for Tumor Therapy via Integrated Cascade Reactions. *Angew. Chem. Int. Ed.* **60**, 9480-9488 (2021).
15. Xu, B. *et al.* A Bioinspired Five-Coordinated Single-Atom Iron Nanozyme for Tumor Catalytic Therapy. *Adv. Mater.* **34**, 2107088 (2022).
16. Zhang, R. *et al.* Edge-Site Engineering of Defective Fe–N4 Nanozymes with Boosted Catalase-Like Performance for Retinal Vasculopathies. *Adv. Mater.* **34**, 2205324 (2022).
17. Liu, W.-J. *et al.* Engineering of Local Coordination Microenvironment in Single-Atom Catalysts Enabling Sustainable Conversion of Biomass into a Broad Range of Amines. *Adv. Mater.* **36**, 2305924 (2024).
18. Lu, X. *et al.* Single-atom catalysts-based catalytic ROS clearance for efficient psoriasis treatment and relapse prevention via restoring ESR1. *Nat. Commun.* **14**, 6767 (2023).
19. Chang, M. *et al.* Cu Single Atom Nanozyme Based High-Efficiency Mild Photothermal Therapy through Cellular Metabolic Regulation. *Angew. Chem. Int. Ed.* **61**, e202209245 (2022).
20. Chen, S. *et al.* High Fe-Loading Single-Atom Catalyst Boosts ROS Production by Density Effect for Efficient Antibacterial Therapy. *Nano-Micro Lett.* **17**, 32 (2024).
21. Chen, Y. *et al.* Atomic-Level Regulation of Cobalt Single-Atom Nanozymes: Engineering High-Efficiency Catalase Mimics. *Angew. Chem. Int. Ed.* **62**, e202301879 (2023).
22. Zhang, J. *et al.* Mn−Ce Symbiosis: Nanozymes with Multiple Active Sites Facilitate Scavenging of Reactive Oxygen Species (ROS) Based on Electron Transfer and Confinement Anchoring. *Angew. Chem. Int. Ed.* **64**, e202416686 (2025).
23. Chen, Z. *et al.* Enzyme-Mimic Activities of RuCo Bimetallic Nanosheets for Inflammatory Bowel Disease Treatment. *J. Am. Chem. Soc.* **147**, 13424-13436 (2025).
24. Li, J. *et al.* Microglial Membranes Wrapped Ultrasmall Medium-Entropy Ru Single-Atom Nanozyme: Enhanced Catalysis for Accelerating Inflammation/Redox Microenvironment Regulation in Intracerebral Hemorrhage. *Adv. Sci.* **n/a**, e20714 (2026).
25. Yuan, L.-J. *et al.* d-Orbital Electron Delocalization Realized by Axial Fe4C Atomic Clusters Delivers High-Performance Fe–N–C Catalysts for Oxygen Reduction Reaction. *Adv. Mater.* **35**, 2305945 (2023).
26. Liu, M. *et al.* Enhancing the ORR durability of single atomic Fe-N4 active sites with implanted SiO2 nanoparticles as radical and H2O2 inhibitors. *Nat. Commun.* **16**, 10178 (2025).
27. Luo, J. *et al.* Engineering Asymmetric and Highly Exposed Fe Single-Atom Nanozymes for siMMP13 Delivery and Ferroptosis Inhibition in Osteoarthritis

Therapy. *Adv. Mater.* **38**, e20951 (2026).
28. Xiao, X. *et al.* A Unique Fe–N4 Coordination System Enabling Transformation of Oxygen into Superoxide for Photocatalytic C□H Activation with High Efficiency and Selectivity. *Adv. Mater.* **34**, 2200612 (2022).
29. Ma, F.-X. *et al.* Impeding Thermal Atomization Enables Synthesizing Fe2N Cluster Liganded Single Fe-Atom Catalyst for Highly Efficient Oxygen Reduction Reaction. *Angew. Chem. Int. Ed.* **64**, e202504935 (2025).
30. Shi, X. *et al.* Metal–support frontier orbital interactions in single-atom catalysis. *Nature* **640**, 668-675 (2025).
31. Cao, S. *et al.* A Library of ROS-Catalytic Metalloenzyme Mimics with Atomic Metal Centers. *Adv. Mater.* **34**, 2200255 (2022).
32. Zhang, P. *et al.* Axial Phosphate Coordination Driven Spin State Change in FeN4 Site for Stable Oxygen Reduction. *Angew. Chem. Int. Ed.* **65**, e24529 (2026).
33. Wang, X., Yi, Z.-Y., Wang, Y.-Q. & Wang, D. Molecular Evidence for the Axial Coordination Effect of Atomic Iodine on Fe-N4 Sites in Oxygen Reduction Reaction. *Angew. Chem. Int. Ed.* **137**, e202413673 (2025).
34. Yang, G. *et al.* Spin polarization regulation of Fe–N4 by Fe3 atomic clusters for highly active oxygen reduction reaction. *Sci. Bull.* **70**, 1793-1803 (2025).
35. Jiang, Z., Tong, K., Li, Z., Tao, H. & Zhu, M. Spin State Regulation for Peroxide Activation: Fundamental Insights and Regulation Mechanisms. *Angew. Chem. Int. Ed.* **137**, e202500791 (2025).
36. Park, S. *et al.* Breaking the Selectivity Barrier of Single-Atom Nanozymes Through Out-of-Plane Ligand Coordination. *Adv. Mater.* **37**, 2506480 (2025).
37. Chen, K. *et al.* Metallothionein-Inspired Asymmetric Heteroatom Doping of Single-Atom Nanozymes for Multi-Enzyme Biocatalysis. *Adv. Sci.* **13**, e17502 (2026).
38. Wang, Q. *et al.* Multi-Hierarchical Fe Single Atom Nanozymes with Axially-Coordinated O-Fe-N4 Active Centers Reshape Macrophage Epigenetics Against Immunosuppression. *Adv. Funct. Mater.* **34**, 2408141 (2024).
39. Yi, K. *et al.* High H2O2 production in membrane-free electrolyzer via anodic bubble shielding towards robust rural disinfection. *Nat. Commun.* **16**, 1893 (2025).
40. Gao, H. *et al.* Precise Axial Coordination Tailors the Spin State of Single-Atom Iron for Boosted Oxygen Reduction Electrocatalysis. *Adv. Funct. Mater.* **n/a**, e31932 (2026).

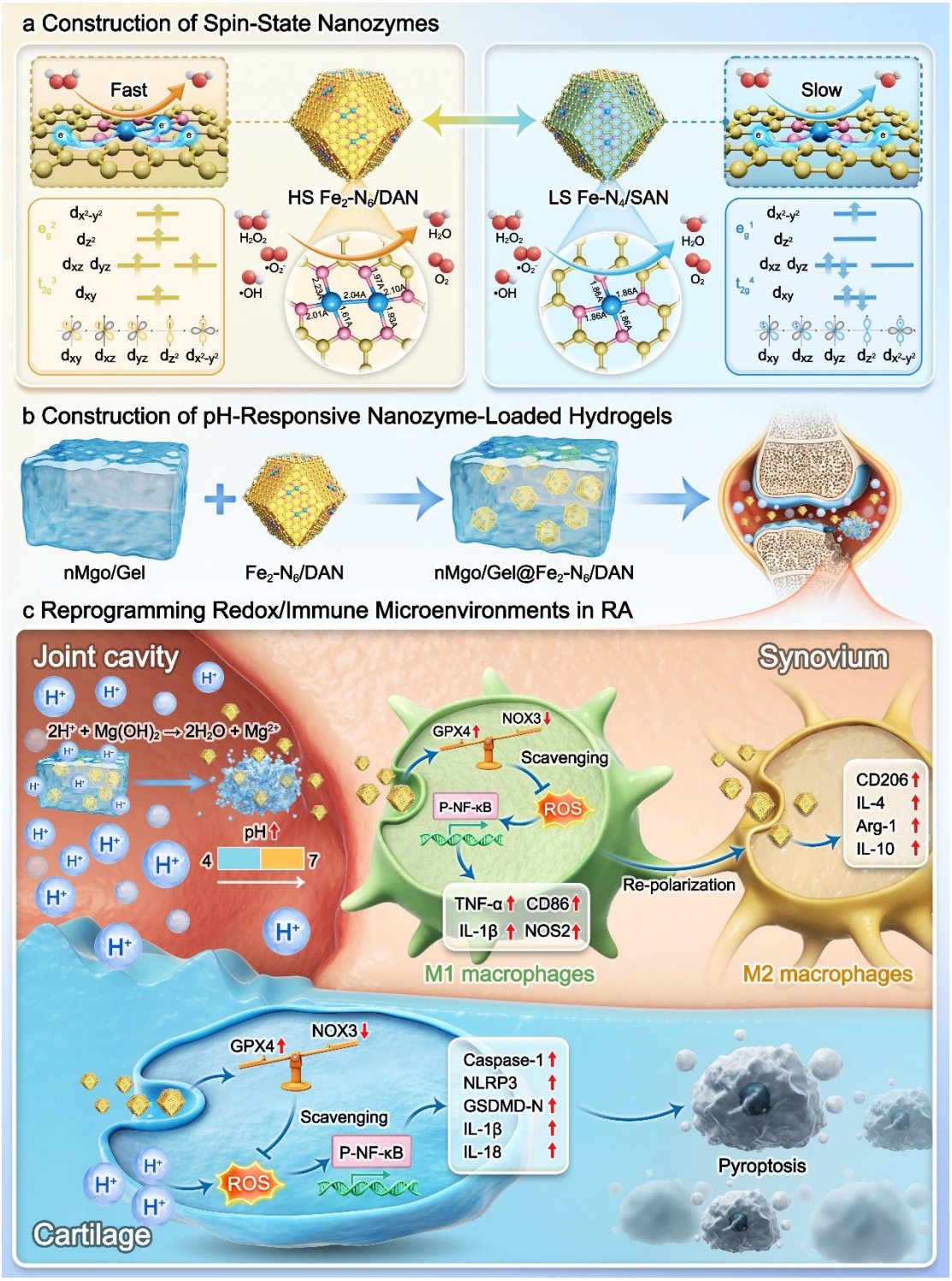


Figure 1. Schematic illustration of synthesis of pH-responsive nMgO/Gel@Fe_2-N_6/DAN and proposed mechanisms: reprogramming redox/immune microenvironments in RA via pyroptosis inhibition.

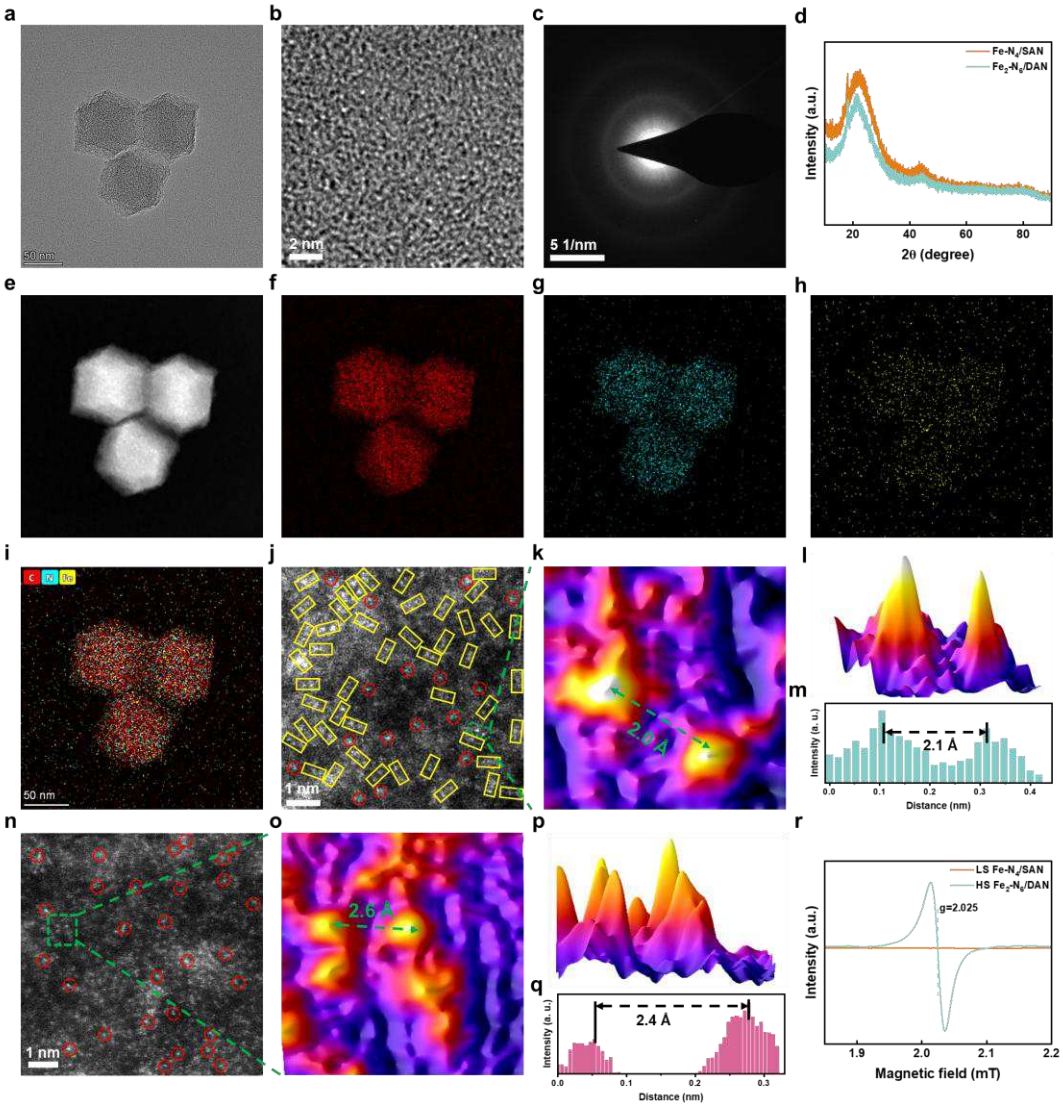


Figure 2. Characterizations of HS Fe_2-N_6/DAN. (a) TEM image of HS Fe_2-N_6/DAN. Scale bar = 50 nm. (b) HR-TEM image of HS Fe_2-N_6/DAN. Scale bar = 2 nm. (c) SAED image of HS Fe_2-N_6/DAN. Scale bar = 5 1/ nm. (d) XRD patterns of HS Fe_2-N_6/DAN and LS Fe-N_4/SAN. (e-i) EDX-Mapping images of HS Fe_2-N_6/DAN. Scale bar = 50 nm. (j) AC HAADF-STEM images of HS Fe_2-N_6/DAN. The isolated dual Fe atoms and single Fe atoms are encircled with yellow boxes and red circles. Scale bar = 1 nm. (k-l) 3D model of HS Fe_2-N_6/DAN bright spots along the green dotted line and (m) the corresponding intensity profiles along the green line. (n) AC HAADF-STEM images of LS Fe-N_4/SAN. The isolated Fe atoms are encircled with red circles. Scale bar = 1 nm. (o-p) 3D model of LS Fe-N_4/SAN bright spots along the green dotted line and (q) the corresponding intensity profiles along the green line. (r) ESR spectra of HS Fe_2-N_6/DAN and LS Fe-N_4/SAN.

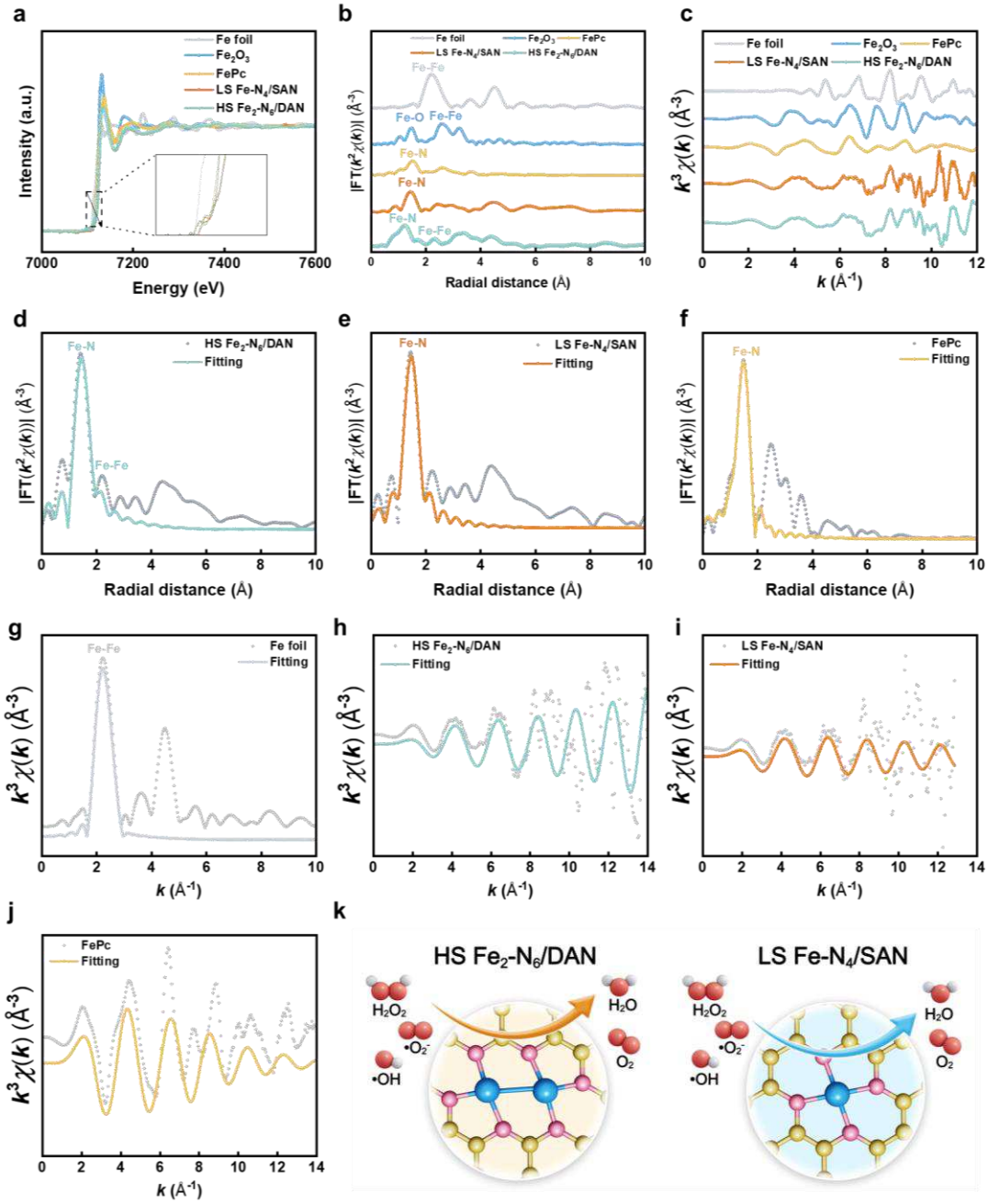


Figure 3. Characterizations of HS Fe_2-N_6/DAN and LS Fe-N_4/SAN. (a) XANES spectra, and matching (b) Fourier transform EXAFS spectra of HS Fe_2-N_6/DAN. and LS Fe-N_4/SAN. (c) EXAFS curves of HS Fe_2-N_6/DAN. and LS Fe-N_4/SAN at the k space. (d) EXAFS fitting curve of HS Fe_2-N_6/DAN, (e) LS Fe-N_4/SAN, (f) FePc, and (g) Fe foil at the R space. (h) EXAFS fitting curves of HS Fe_2-N_6/DAN, (i) LS Fe-N_4/SAN, and (j) FePc at the k space. (k) The structural and biocatalytic advantages of HS Fe_2-N_6/DAN and LS Fe-N_4/SAN.

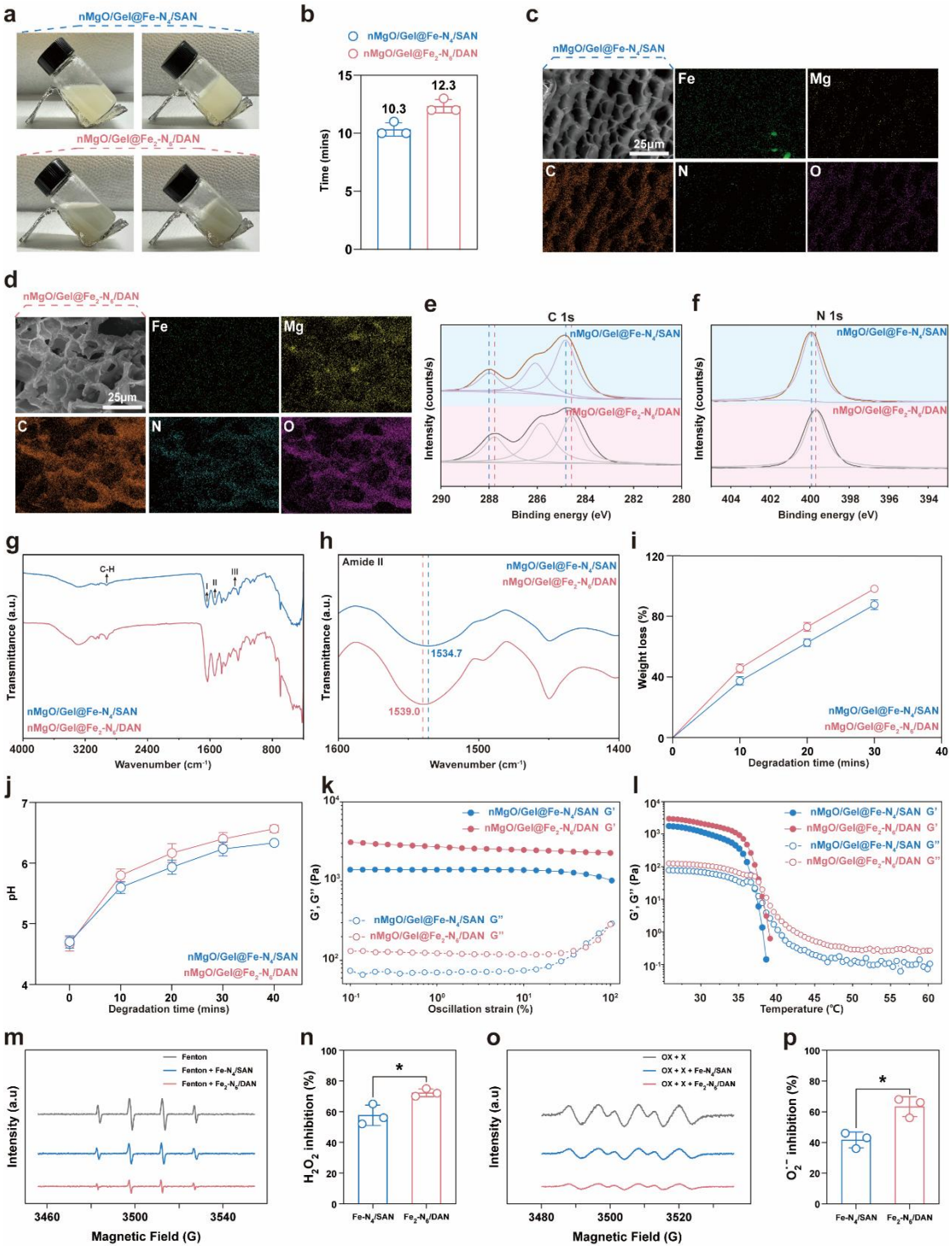


Figure 4. Characterization and multiple enzyme-like activities of nMgO/Gel@Fe-N4/SAN and nMgO/Gel@Fe2-N6/DAN. (a-b) Gelation behavior and gelation time of nMgO/Gel@Fe-N4/SAN and nMgO/Gel@Fe2-N6/DAN hydrogels. (c-d) EDS elemental mapping images of nMgO/Gel@Fe-N4/SAN and nMgO/Gel@Fe2-N6/DAN hydrogels. Scale bar:25 μm. (e-f) XPS narrow-spectra with fitting curves of C 1s, and N 1s for composites. (g-h) FTIR spectra of nMgO/Gel@Fe-N4/SAN and

nMgO/Gel@Fe_2-N_6/DAN hydrogels. (i-j) Degradation and variation in the pH of nMgO/Gel@Fe-N_4/SAN and nMgO/Gel@Fe_2-N_6/DAN hydrogels after soaking in PBS for various time periods. n = 3 per group. (k-l) The strain sweep curves and temperature ramp curves of nMgO/Gel@Fe-N_4/SAN and nMgO/Gel@Fe_2-N_6/DAN hydrogels. (m) •OH scavenging property by ESR. (n) Inhibition rates of H_2O_2 of different groups. n = 3 per group. (o) $•O_2^-$ scavenging property by ESR. (p) Inhibition rates of $•O_2^-$ of different groups. n = 3 per group. All data represent Mean ± SD. *P < 0.05.

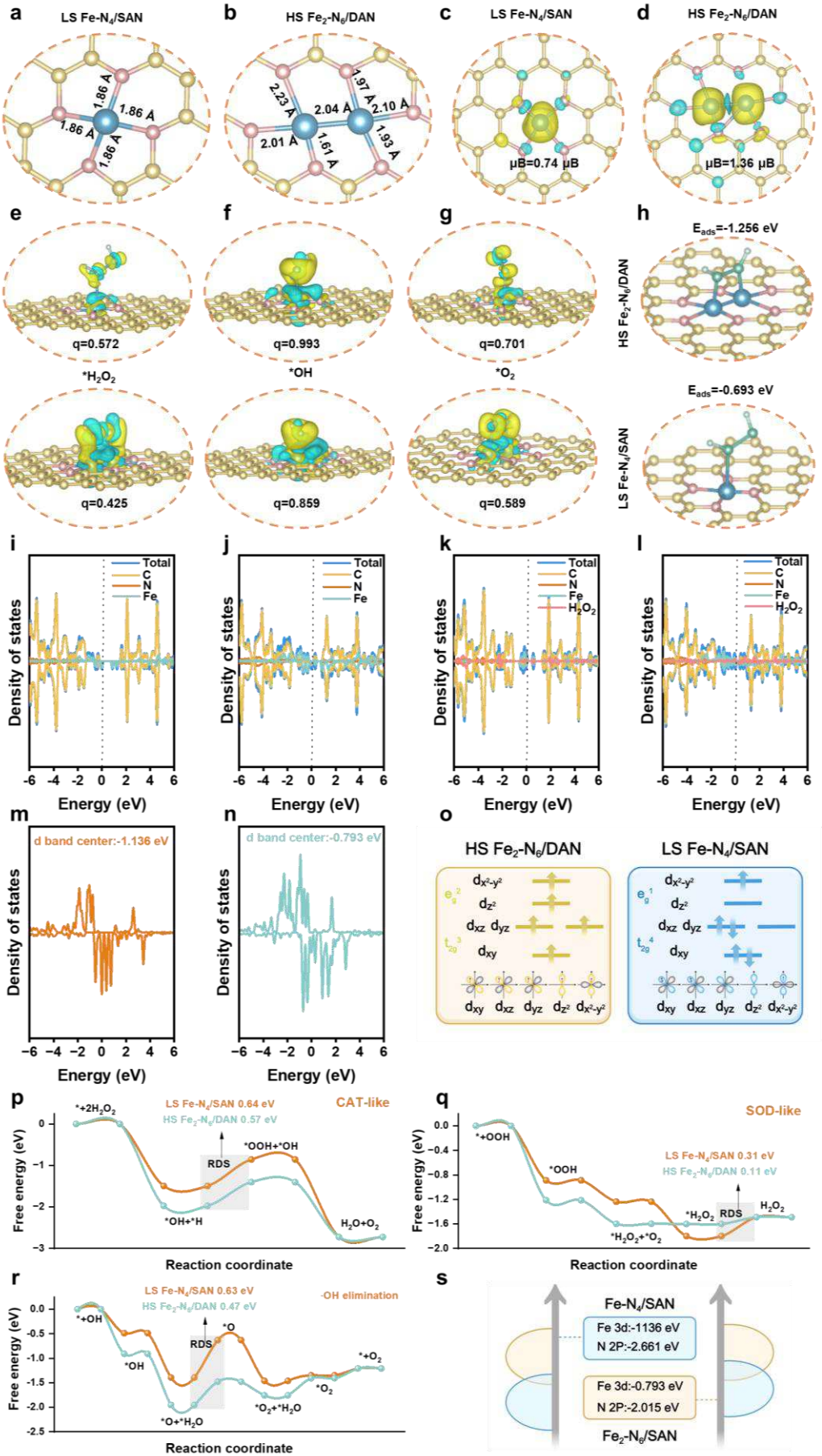

a
LS Fe-N4/SAN
1.86 Å
1.86 Å
1.86 Å
1.86 Å
b
HS Fe2-N6/DAN
2.23 Å
2.04 Å
1.97 Å
2.10 Å
2.01 Å
1.61 Å
1.93 Å
c
LS Fe-N4/SAN
μB=0.74 μB
d
HS Fe2-N6/DAN
μB=1.36 μB
e
q=0.572
*H2O2
f
q=0.993
*OH
g
q=0.701
*O2
h
Eads=-1.256 eV
HS Fe2-N6/DAN
Eads=-0.693 eV
LS Fe-N4/SAN
q=0.425
q=0.859
q=0.589
i
j
k
l
Total
C
N
Fe
H2O2
Density of states
Energy (eV)
m
d band center:-1.136 eV
n
d band center:-0.793 eV
o
HS Fe2-N6/DAN
LS Fe-N4/SAN
dx²-y²
dz²
dxz dyz
dxy
eg²
t2g³
eg¹
t2g⁴
p
LS Fe-N4/SAN 0.64 eV
HS Fe2-N6/DAN 0.57 eV
CAT-like
*+2H2O2
*OOH+*OH
RDS
*OH+*H
H2O+O2
Free energy (eV)
Reaction coordinate
q
SOD-like
*+OOH
*OOH
LS Fe-N4/SAN 0.31 eV
HS Fe2-N6/DAN 0.11 eV
*H2O2
RDS
H2O2
*H2O2+*O2
r
LS Fe-N4/SAN 0.63 eV
HS Fe2-N6/DAN 0.47 eV
-OH elimination
*+OH
*O
*OH
*+O2
*O2
*O2+*H2O
*O+*H2O
s
Fe-N4/SAN
Fe 3d:-1136 eV
N 2P:-2.661 eV
Fe 3d:-0.793 eV
N 2P:-2.015 eV
Fe2-N6/SAN

Figure 5. DFT calculation and catalytic mechanism of HS Fe_2-N_6/DAN and LS Fe-N_4/SAN. (a) Optimized structure and bond lengths in symmetric LS Fe-N_4/SAN and (b) asymmetric HS Fe_2-N_6/DAN. (c) Total magnetic moments Fe atoms in symmetric LS Fe-N_4/SAN and (d) asymmetric HS Fe_2-N_6/DAN. (e-g) The CDD and Bader charge of HS Fe_2-N_6/DAN (up) or LS Fe-N_4/SAN (down) structures upon adsorption of *H_2O_2, *•OH and *•O_2^- with an isosurface value set at 0.003 e/Å^3, yellow represents the accumulation area of electrons, while blue represents the dissipation area of electrons. (h) E_{ads} for H_2O_2, for asymmetric HS Fe_2-N_6/DAN (up) and symmetric LS Fe-N_4/SAN (down). (i) DOS analysis of Fe, C, and N atoms in LS Fe-N_4/SAN and (j) HS Fe_2-N_6/DAN. (k) DOS analysis of Fe, C, and N atoms in H_2O_2-adsorbed LS Fe-N_4/SAN and (l) H_2O_2-adsorbed HS Fe_2-N_6/DAN. (m) DOS analysis of Fe 3d band center atoms in LS Fe-N_4/SAN and (n) HS Fe_2-N_6/DAN. (o) Optimizing the distribution of electronic spin states on HS Fe_2-N_6/DAN and LS Fe-N_4/SAN. (p) Gibbs free-energy diagrams for the decomposition of H_2O_2 into O_2, (q) the conversion of •O_2^- into H_2O_2, and (r) the conversion of •OH into H_2O on HS Fe_2-N_6/DAN and LS Fe-N_4/SAN. (s) Optimizing the binding strength of oxygen species on HS Fe_2-N_6/DAN and LS Fe-N_4/SAN.

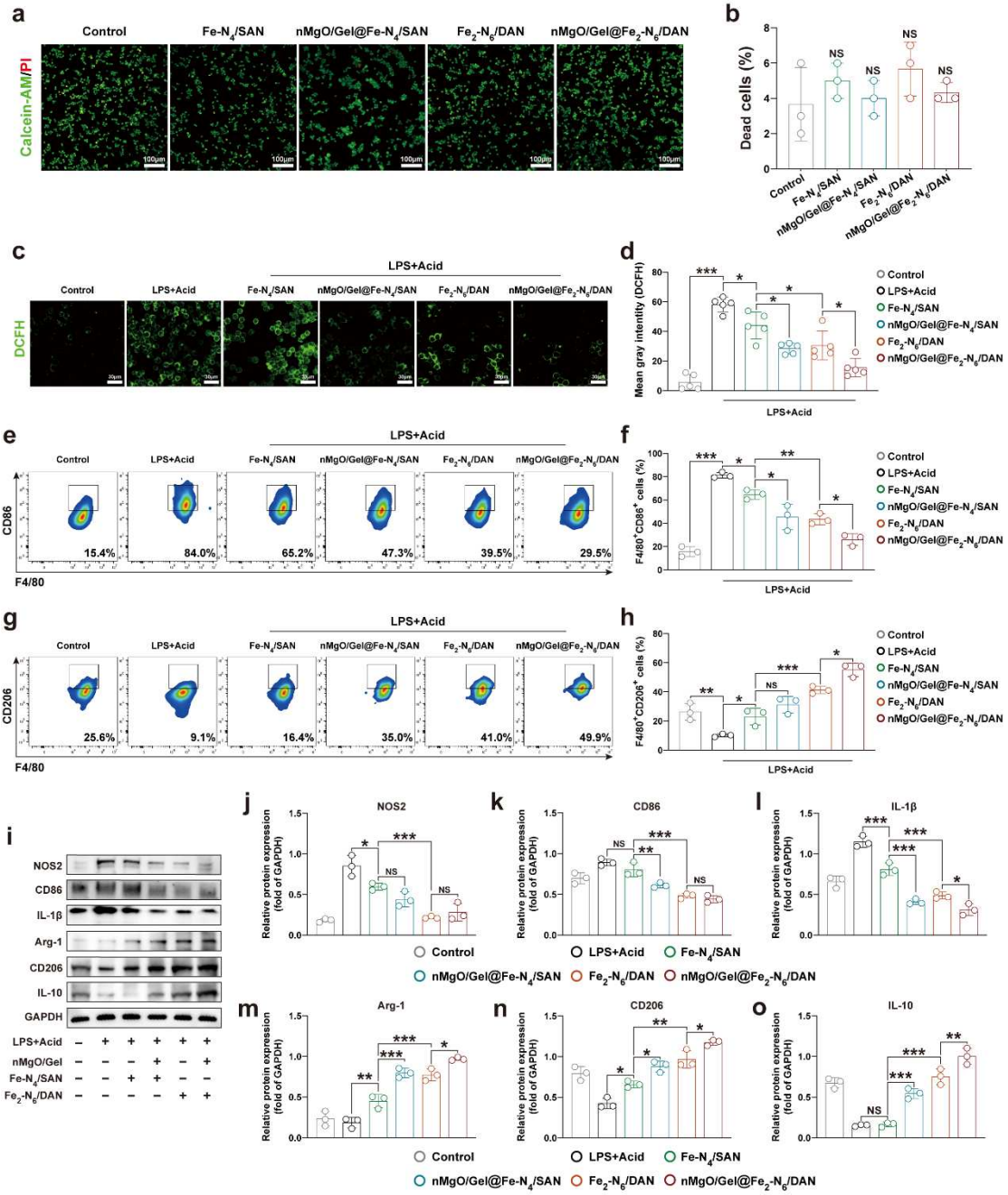


Figure 6. Scavenging ROS and subsequent reprogramming on macrophages by nMgO/Gel@Fe$_2$-N$_6$/DAN in vitro. (a-b) Representative fluorescence images and quantification of various treatments on BMDMs stained with Calcein-AM/PI. Green and red represent live and dead cells respectively. Scale bar: 100 μm. n = 3 per group. (c-d) Representative fluorescence images and quantifications of various treatments of BMDMs stained with DCFH-DA (green). Scale bar: 30 μm. n = 5 per group. (e-f) Flow cytometry analyses and corresponding quantifications of F4/80$^+$CD86$^+$ BMDMs after different treatments. n = 3 per group. (g-h) Flow cytometry analyses and corresponding quantifications of F4/80$^+$CD206$^+$ BMDMs after different treatments. n = 4 per group.

(i-o) Western blot analysis and quantifications of NOS2, CD86, CD206, IL-1β, Arg-1, CD206 and IL-10 in various treatments of BMDMs. n = 3 per group. All data represent Mean ± SD. NS = not significant. *P < 0.05, **P < 0.01, ***P < 0.001.

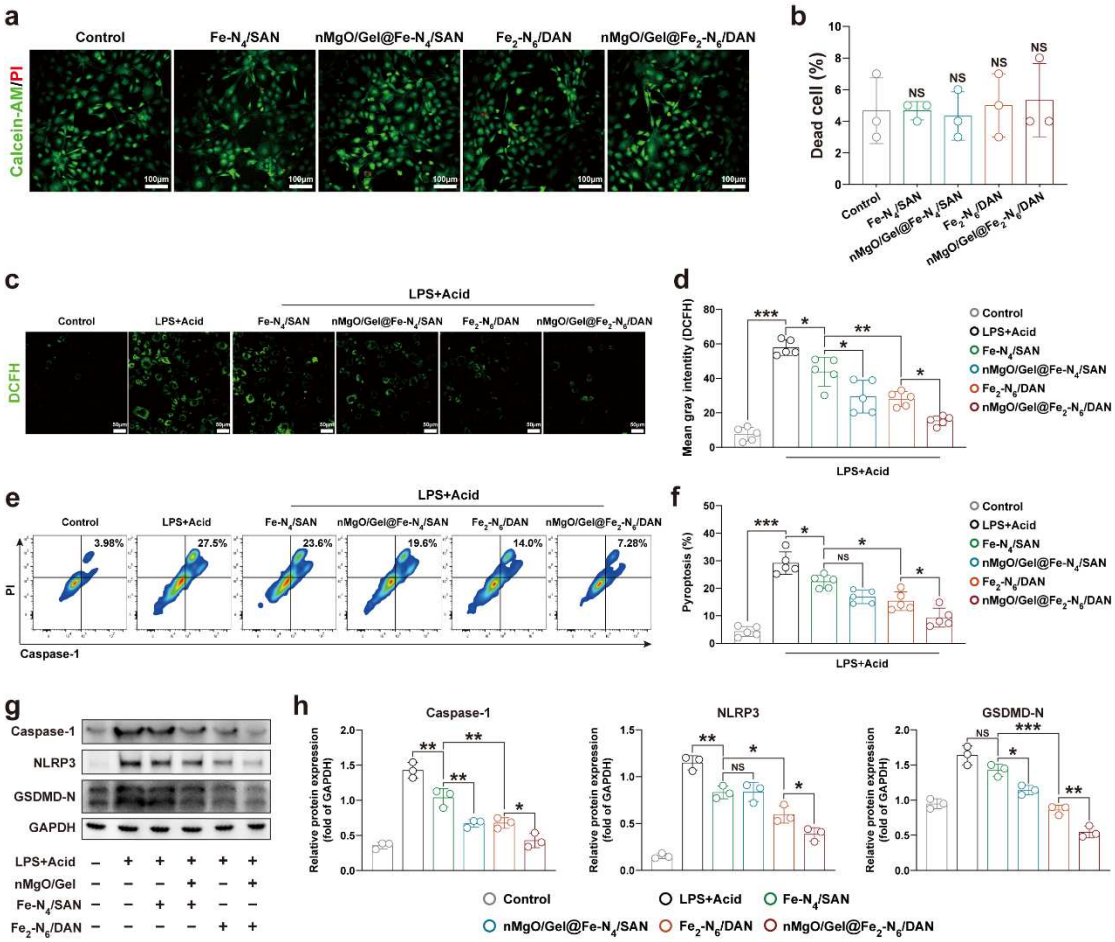


Figure 7. Scavenging of ROS and subsequent inhibition of pyroptosis on chondrocytes by nMgO/Gel@Fe$_2$-N$_6$/DAN in vitro. (a-b) Representative fluorescence images and quantification of various treatments on chondrocytes stained with Calcein-AM/PI. Green and red represent live and dead cells respectively. Scale bar: 100 μm. n = 3 per group. (c-d) Representative fluorescence images and quantifications of various treatments of chondrocytes stained with DCFH-DA (green). Scale bar: 50 μm. n = 5 per group. (e-f) Flow cytometry analyses and corresponding quantifications of Cacpase-1$^+$PI$^+$ chondrocytes after different treatments. n = 5 per group. (g-h) Western blot analysis and quantifications of Caspase-1, NLRP3 and GSDMD-N in various treatments of chondrocytes. n = 3 per group. All data represent Mean ± SD. NS = not significant. *P < 0.05, **P < 0.01, ***P < 0.001.

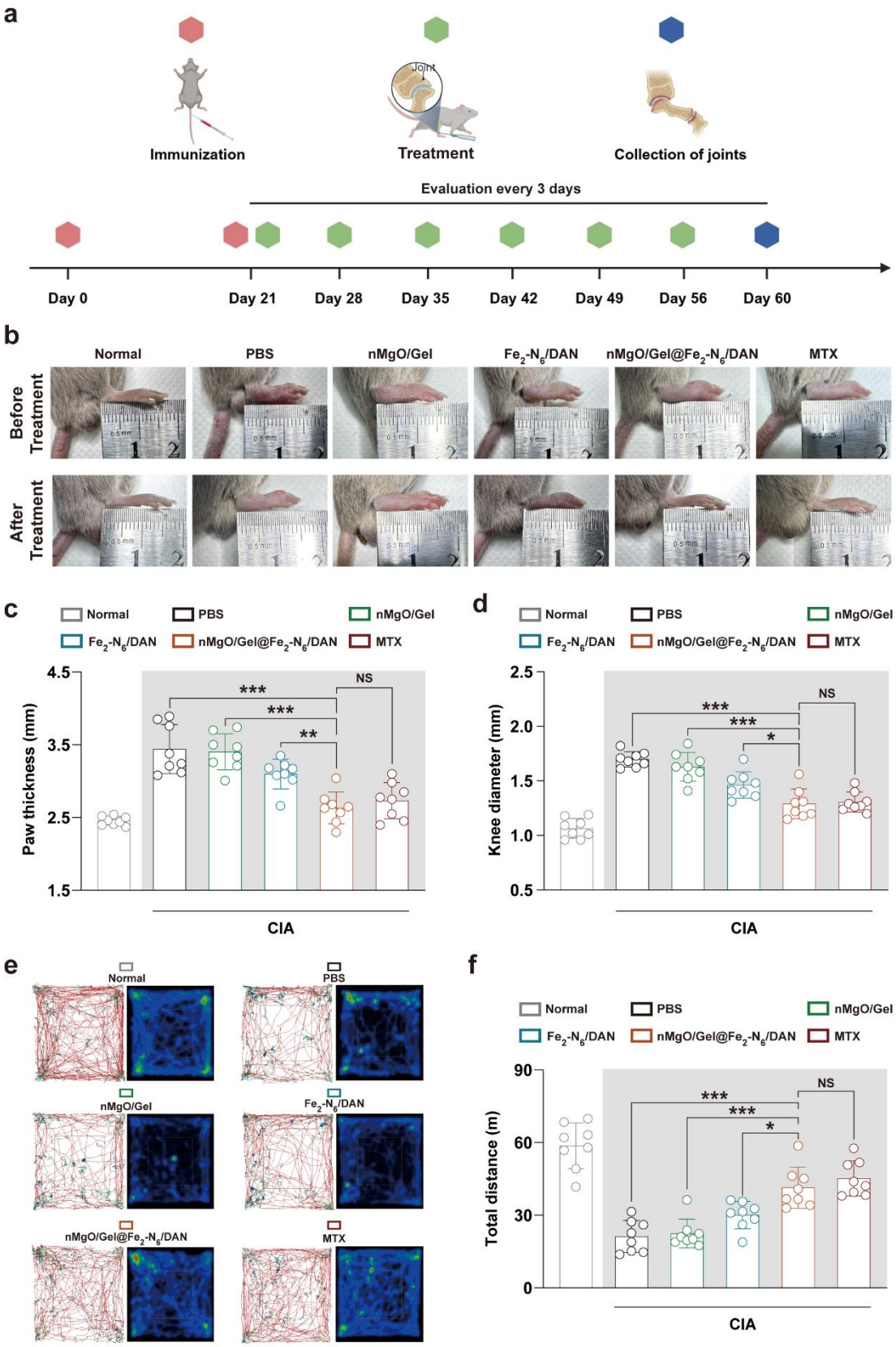


Figure 8. nMgO/Gel@Fe_2-N_6/DAN demonstrates therapeutic efficacy in CIA mice. (a) The schematic illustration of nMgO/Gel@Fe_2-N_6/DAN treatment. (b) Visual

documentation of articular morphology changes in CIA mice before and after different treatment. (c-d) Statistical comparison of paw thickness and knee diameter among treatment groups at day 60 post-immunization. (e) Representative images of open field test of CIA mice with different treatment. (f) Quantified analysis of total distance of CIA mice with different treatment. n = 8 per group. All data represent Mean ± SD. NS = not significant. *P < 0.05, **P < 0.01, ***P < 0.001.

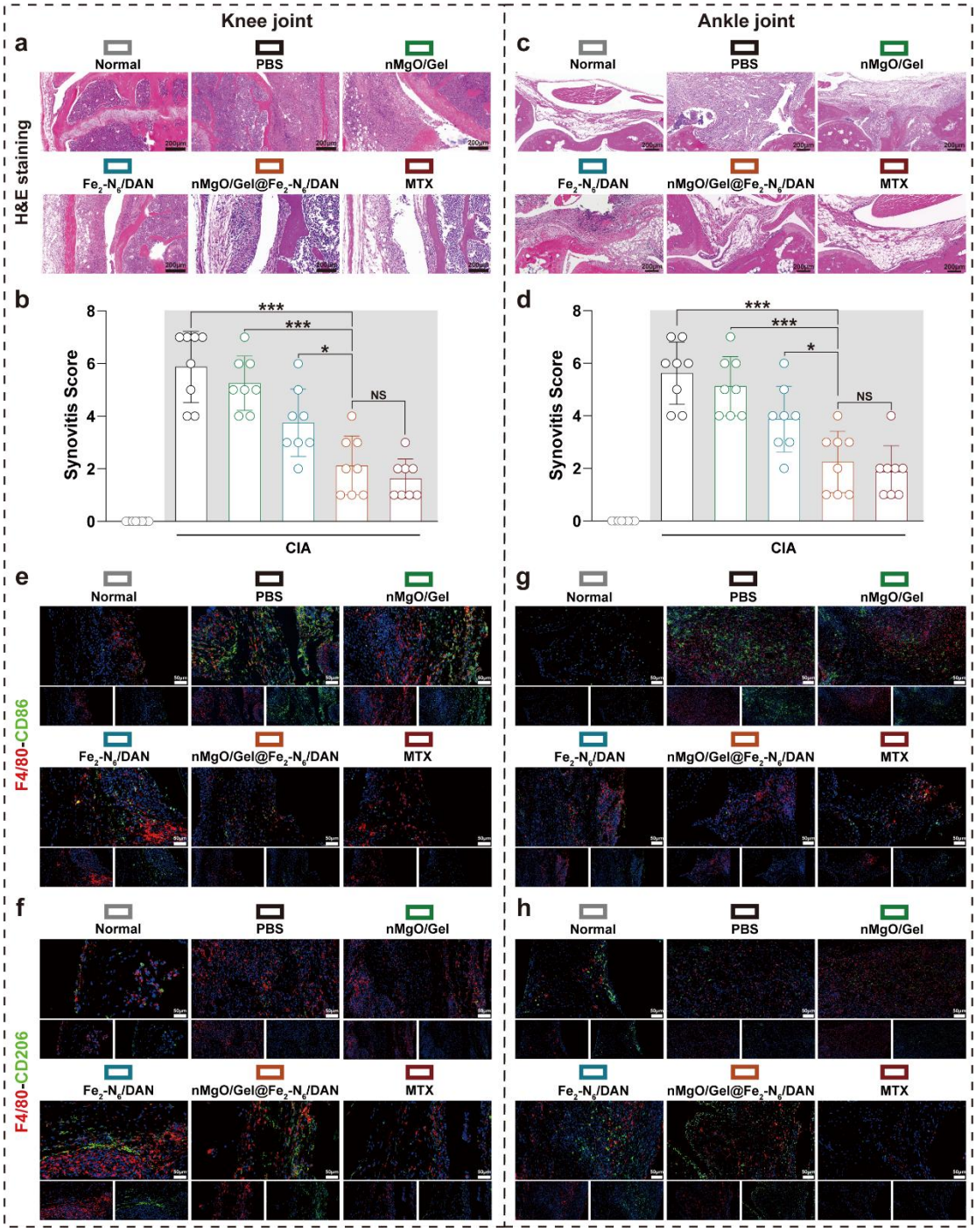


Figure 9. nMgO/Gel@Fe$_2$-N$_6$/DAN alleviates synovitis and modulates macrophage polarization in CIA mice. (a-d) Representative images and quantitative assessment of H&E-stained knee and ankle joint sections from CIA mice across treatment groups. Scale bar: 200 μm. (e-h) Representative immunofluorescence staining of F4/80 and CD86/CD206 in knee and ankle joint sections from CIA mice across treatment groups. Scale bar: 50 μm. n = 8 per group. All data represent Mean ± SD. NS = not significant. *P < 0.05, **P < 0.01, ***P < 0.001.

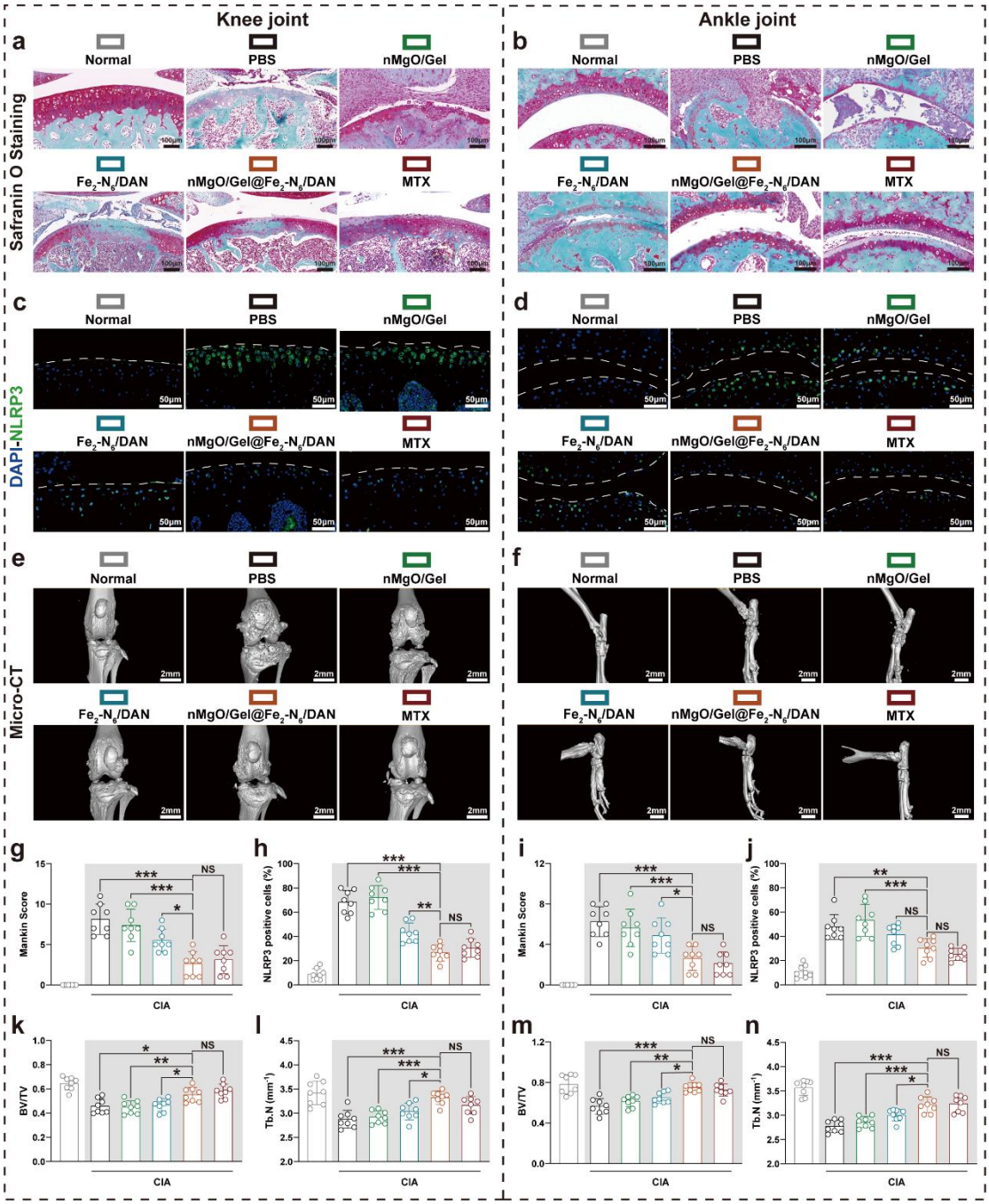


Figure 10. Treatment of nMgO/Gel@Fe2-N6/DAN mitigates cartilage pyroptosis and bone erosion in CIA mice. (a, b, g, i) Representative images and quantified analysis of safranin O and fast green staining in the knee and ankle joints of CIA mice with different treatment. Scale bar: 100 μm. n = 8 per group. (c, d, h, j) Representative immunofluorescence staining of NLRP3 (green) and quantitative analysis of coimmunostaining of NLRP3+ cells in the cartilage of the knee and ankle joints from CIA mice with different treatment. Scale bar: 50 μm. n = 8 per group. (e, f, k-n) Representative images and quantified analysis of micro-CT in the knee and ankle joints

of CIA mice with different treatment. Scale bar: 2 mm. n = 8 per group. All data represent Mean ± SD. NS = not significant. *P < 0.05, **P < 0.01, ***P < 0.001.

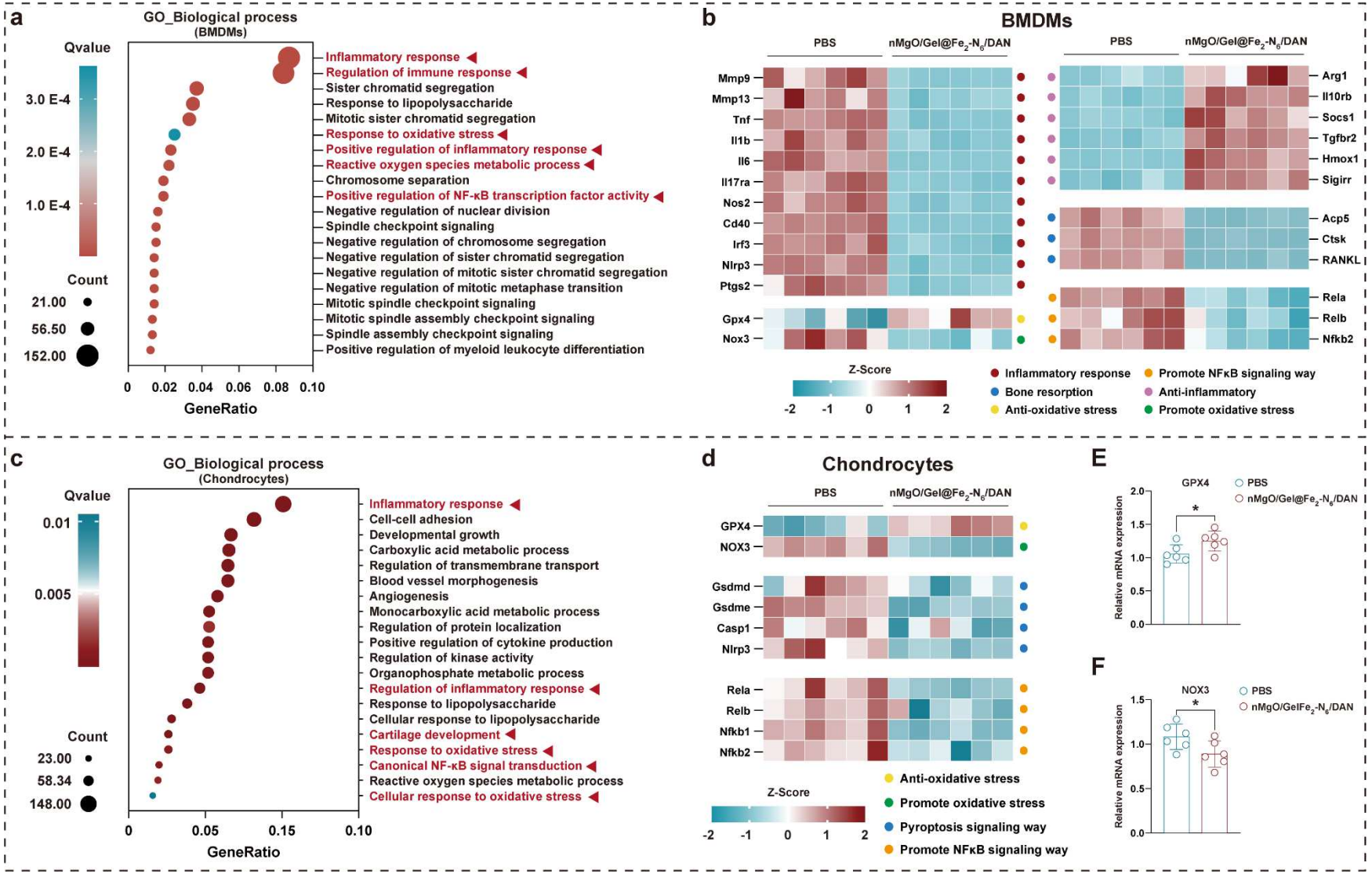

a
GO_Biological process
(BMDMs)
Qvalue
3.0 E-4
2.0 E-4
1.0 E-4
Count
21.00
56.50
152.00
Inflammatory response
Regulation of immune response
Sister chromatid segregation
Response to lipopolysaccharide
Mitotic sister chromatid segregation
Response to oxidative stress
Positive regulation of inflammatory response
Reactive oxygen species metabolic process
Chromosome separation
Positive regulation of NF-κB transcription factor activity
Negative regulation of nuclear division
Spindle checkpoint signaling
Negative regulation of chromosome segregation
Negative regulation of sister chromatid segregation
Negative regulation of mitotic sister chromatid segregation
Negative regulation of mitotic metaphase transition
Mitotic spindle checkpoint signaling
Mitotic spindle assembly checkpoint signaling
Spindle assembly checkpoint signaling
Positive regulation of myeloid leukocyte differentiation
0 0.02 0.04 0.06 0.08 0.10
GeneRatio
b
BMDMs
PBS
nMgO/Gel@Fe2-N6/DAN
Mmp9
Mmp13
Tnf
Il1b
Il6
Il17ra
Nos2
Cd40
Irf3
Nlrp3
Ptgs2
Gpx4
Nox3
Arg1
Il10rb
Socs1
Tgfbr2
Hmox1
Sigirr
Acp5
Ctsk
RANKL
Rela
Relb
Nfkb2
Z-Score
-2 -1 0 1 2
Inflammatory response
Bone resorption
Anti-oxidative stress
Promote NFκB signaling way
Anti-inflammatory
Promote oxidative stress
c
GO_Biological process
(Chondrocytes)
Qvalue
0.01
0.005
Count
23.00
58.34
148.00
Inflammatory response
Cell-cell adhesion
Developmental growth
Carboxylic acid metabolic process
Regulation of transmembrane transport
Blood vessel morphogenesis
Angiogenesis
Monocarboxylic acid metabolic process
Regulation of protein localization
Positive regulation of cytokine production
Regulation of kinase activity
Organophosphate metabolic process
Regulation of inflammatory response
Response to lipopolysaccharide
Cellular response to lipopolysaccharide
Cartilage development
Response to oxidative stress
Canonical NF-κB signal transduction
Reactive oxygen species metabolic process
Cellular response to oxidative stress
0 0.05 0.15 0.10
GeneRatio
d
Chondrocytes
PBS
nMgO/Gel@Fe2-N6/DAN
GPX4
NOX3
Gsdmd
Gsdme
Casp1
Nlrp3
Rela
Relb
Nfkb1
Nfkb2
Z-Score
-2 -1 0 1 2
Anti-oxidative stress
Promote oxidative stress
Pyroptosis signaling way
Promote NFκB signaling way
E
GPX4
PBS
nMgO/Gel@Fe2-N6/DAN
Relative mRNA expression
2.0
1.5
1.0
0.5
0.0
*
F
NOX3
PBS
nMgO/GelFe2-N6/DAN
Relative mRNA expression
1.5
1.0
0.5
0.0
*

Figure 11. The RNA-seq analysis of BMDMs or chondrocytes treated with nMgO/Gel@Fe_2-N_6/DAN and exposed to acidic and LPS conditions. (a) Representative GO analysis (biological process) of DEGs in the BMDMs from nMgO/Gel@Fe_2-N_6/DAN vs. PBS (|log2FC| ≥ 1). (b) DEGs contributing to GO enrichment analysis in the BMDMs from nMgO/Gel@Fe_2-N_6/DAN vs. PBS. Heatmap of selected significantly upregulated and downregulated genes depicting standardized gene expression values (z-scores) in the BMDMs from nMgO/Gel@Fe_2-N_6/DAN vs. PBS. Individual biological replicates are shown (n = 6). Genes are classified according to known functions indicated by the colored circles next to the heat map. (c) Representative GO analysis (biological process) of DEGs in the chondrocytes from nMgO/Gel@Fe_2-N_6/DAN vs. PBS (|log2FC| ≥ 1). (d) DEGs contributing to GO enrichment analysis in the chondrocytes from nMgO/Gel@Fe_2-N_6/DAN vs. PBS. Heatmap of selected significantly upregulated and downregulated genes depicting standardized gene expression values (z-scores) in the chondrocytes from nMgO/Gel@Fe_2-N_6/DAN vs. PBS. Individual biological replicates are shown (n = 6). Genes are classified according to known functions indicated by the colored circles next to the heat map. (e-f) qRT-PCR analysis of GPX4 (E) and NOX3 (F) relative mRNA expression in chondrocytes from nMgO/Gel@Fe_2-N_6/DAN vs. PBS. n = 6 per group. All data represent Mean ± SD. *P < 0.05.

Supplementary Files

This is a list of supplementary files associated with this preprint. Click to download.

- SupplementaryInformation.docx